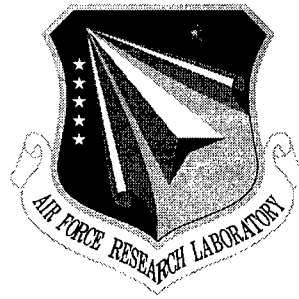


AFRL-SN-RS-TR-1999-260
Final Technical Report
January 2000



**DEVICE & SYSTEM RESEARCH IN MILLIMETER
WAVE FIBER-OPTIC LINK & DISTRIBUTED
ANTENNA NETWORKS FOR CELLULAR AND
PERSONAL COMMUNICATIONS**

University of California, Berkeley

Sponsored by
Defense Advanced Research Projects Agency
DARPA Order No. C552

APPROVED FOR PUBLIC RELEASE; DISTRIBUTION UNLIMITED.

The views and conclusions contained in this document are those of the authors and should not be interpreted as necessarily representing the official policies, either expressed or implied, of the Defense Advanced Research Projects Agency or the U.S. Government.

20000308 016

AIR FORCE RESEARCH LABORATORY
SENSORS DIRECTORATE
ROME RESEARCH SITE
ROME, NEW YORK

DTIC QUALITY INSPECTED 3

This report has been reviewed by the Air Force Research Laboratory, Information Directorate, Public Affairs Office (IFOIPA) and is releasable to the National Technical Information Service (NTIS). At NTIS it will be releasable to the general public, including foreign nations.

AFRL-SN-RS-TR-1999-260 has been reviewed and is approved for publication.

APPROVED: *James R. Hunter*
JAMES R. HUNTER
Project Engineer

FOR THE DIRECTOR: *Robert G. Polce*
ROBERT G. POLCE, Acting Chief
Rome Operations Office

If your address has changed or if you wish to be removed from the Air Force Research Laboratory Rome Research Site mailing list, or if the addressee is no longer employed by your organization, please notify AFRL/SNDR, 25 Electronics Pky, Rome, NY 13441-4515. This will assist us in maintaining a current mailing list.

Do not return copies of this report unless contractual obligations or notices on a specific document require that it be returned.

DEVICE & SYSTEM RESEARCH IN MILLIMETER WAVE FIBER-OPTIC LINK &
DISTRIBUTED ANTENNA NETWORKS FOR CELLULAR AND PERSONAL
COMMUNICATIONS

Kam Lau

Contractor: University of California, Berkeley
Contract Number: F30602-95-C-0116
Effective Date of Contract: 16 June 1995
Contract Expiration Date: 31 December 1998
Program Code Number: 6D10
Short Title of Work: Device & System Research in Millimeter
Wave Fiber-Optic Link & Distributed
Antenna Networks For Cellular And
Personal Communications
Period of Work Covered: Jun 95 - Dec 98
Principal Investigator: Kam Lau
Phone: (510) 642-6251
AFRL Project Engineer: James R. Hunter
Phone: (315) 330-7045

APPROVED FOR PUBLIC RELEASE; DISTRIBUTION UNLIMITED.

This research was supported by the Defense Advanced Research
Projects Agency of the Department of Defense and was monitored
by James R. Hunter, AFRL/SNDR, 25 Electronic Pky, Rome, NY.

REPORT DOCUMENTATION PAGE			Form Approved OMB No. 0704-0188	
Public reporting burden for this collection of information is estimated to average 1 hour per response, including the time for reviewing instructions, searching existing data sources, gathering and maintaining the data needed, and completing and reviewing the collection of information. Send comments regarding this burden estimate or any other aspect of this collection of information, including suggestions for reducing this burden, to Washington Headquarters Services, Directorate for Information Operations and Reports, 1215 Jefferson Davis Highway, Suite 1204, Arlington, VA 22202-4302, and to the Office of Management and Budget, Paperwork Reduction Project (0704-0188), Washington, DC 20503.				
1. AGENCY USE ONLY (Leave blank)		2. REPORT DATE JANUARY 2000		3. REPORT TYPE AND DATES COVERED FINAL Jun 95 - Dec 98
4. TITLE AND SUBTITLE DEVICE & SYSTEM RESEARCH IN MILLIMETER WAVE FIBER-OPTIC LINK & DISTRIBUTED ANTENNA NETWORKS FOR CELLULAR AND PERSONAL COMMUNICATIONS			5. FUNDING NUMBERS C - F30602-95-C-0116 PE - 61101E PR - C552 TA - 00 WU - 01	
6. AUTHOR(S) Kam Lau				
7. PERFORMING ORGANIZATION NAME(S) AND ADDRESS(ES) University of California, Berkeley Electronics Research Laboratory 253 Cory Hall #1774 Berkeley CA 94720			8. PERFORMING ORGANIZATION REPORT NUMBER N/A	
9. SPONSORING/MONITORING AGENCY NAME(S) AND ADDRESS(ES) Defense Advanced Research Projects Agency Air Force Research Laboratory/SNDR 3701 North Fairfax Drive 25 Electronic Pkwy Arlington VA 22203-1714 Rome NY 13441-4515			10. SPONSORING/MONITORING AGENCY REPORT NUMBER AFRL-SN-RS-TR-1999-260	
11. SUPPLEMENTARY NOTES Air Force Research Laboratory Project Engineer: James R. Hunter/SNDR/(315) 330-7045				
12a. DISTRIBUTION AVAILABILITY STATEMENT APPROVED FOR PUBLIC RELEASE; DISTRIBUTION UNLIMITED.			12b. DISTRIBUTION CODE	
13. ABSTRACT (Maximum 200 words) Device and system aspect of distributed antenna systems were investigated for supporting wireless communications in an in-building environment. The infrastructure is fiber-based, but with the key criterion of being low-cost. From the device end, VCSELs were investigated as optical sources for the fiber-optic network, since these devices are being mass-manufactured for fiber-network applications. From the systems end, a "saturated" antenna architecture was investigated for bringing about highest cost/performance ratio. This architecture negates the need for performing site-specific planning and survey, thus greatly reducing the cost of installation of the system. The experimental, simulation and analytical approaches employed in these studies led to a solid understanding of the performance of such a network and its dependence on various parameters of the devices and systems.				
14. SUBJECT TERMS Distributed Antenna, VCSELs, Antenna Architecture, In-Building Wireless System			15. NUMBER OF PAGES 68	
			16. PRICE CODE	
17. SECURITY CLASSIFICATION OF REPORT UNCLASSIFIED	18. SECURITY CLASSIFICATION OF THIS PAGE UNCLASSIFIED	19. SECURITY CLASSIFICATION OF ABSTRACT UNCLASSIFIED	20. LIMITATION OF ABSTRACT UL	

TABLE OF CONTENTS

Abstract of Final Report	1
1. RF Photonics by VCSELS with Embedded Quantum-well Absorber	2
1.1 Introduction	2
1.2 Device Structure	4
1.3 Negative Differential Resistance	5
1.4 Optical Bistability	7
1.5 Self-pulsation	8
1.6 Absorber Modulation	11
1.6.1 Experimental Results	11
1.6.2 Discussion of Frequency Chirp	12
1.6.3 Design Criteria	14
1.7 Conclusions	15
1.8 Section Reference	16
2. In-Building Radio Distribution Using a Saturated Distributed-Antenna Architecture	18
2.1 Introduction	18
2.2 “Saturated” Distributed-antenna Architecture	19
2.3 In-Building Radio Modeling and Simulation	20
2.4 Statistical RF Modeling of In-Building Distributed-Antenna System	21
2.4.1 Statistical Versus “Exact” Approaches	21
2.4.2 Equivalent-Grid Model	23
2.5 Results	25
2.6 Further Discussions	30
2.7 Conclusions	32
2.8 Section Reference	33
3. In-Building Radio Distribution Using a “Saturated” Distributed-Antenna Architecture – Analytic Approach	35
3.1 Introduction	35
3.2 Empty Cell Model	37
3.2.1 Rayleigh’s Random Flights	37

3.2.2 Probability Density Function of RF amplitude Distribution Inside Cell	38
3.2.3 PDF For Two Special Cases	40
3.2.4 Central Limit Interpretation	41
3.3 Cell with Grid Walls	42
3.3.1 Analysis with no Images	43
3.3.2 Analysis with a Uniform Distribution of Image Antennae	44
3.3.3 Rigorous Treatment of Image Antennae	44
3.4 Comparison with Simulation	45
3.5 Conclusion	48
3.6 Appendix: Proof of Convergence	49
3.7 Section Reference	51

LIST OF FIGURES

Fig 1a. Device schematic	4
Fig 1b. Electronic bias circuit for optical bistability and self-pulsation	5
Fig 1c. Electronic bias circuit for absorber modulation	5
Fig 2a. Absorber current vs. voltage (I_a - V_a) traces for device A	6
Fig 2b. Absorber current vs. voltage (I_a - V_a) traces for device B	6
Fig 3a. Origin of the sharp region of negative differential resistance in the absorber I-V trace	7
Fig 3b. The absorber IV trace resulting from the sweeping of the absorption Peak in Fig 3a	7
Fig 4a. Bistable operation	8
Fig 4b. Bistable operation	8
Fig 5a. Self-pulsation regime	8
Fig 5b. Self-pulsation regime: the L - I_g trace	8
Fig 6a. Self-pulsation OFF	10
Fig 6b. Self-pulsation ON	10
Fig 6c. Self-pulsation ON: RF spectrum enlarged	10
Fig 7. Tuning of the self-pulsation frequency by adjusting the gain bias current I_g	10
Fig 8. L - I_g and V_g - I_g for a typical Device A with absorber voltage $V_a=0$	11
Fig 9a. Absorber modulation response for fixed DC absorber bias and varying Laser bias current	12
Fig 9b. L - I_g and V_g - I_g for a typical Device A with absorber voltage $V_a=0$	12
Fig 10. Absorber modulation response for fixed gain bias and varying DC bias	12
Fig 11. Predicted effect of absorber and direct modulation on carrier density	14
Fig 12. Transformation from original floor plan to equivalent grid	23
Fig 13. Three floor plans with different average wall separation	24
Fig 14. Radio Statistics for different d , R , T	26
Fig 15. Radio statistics comparison for two floor plans with different antennas	27
Fig 16. PDF obtained from ray-tracing of actual floor plan, and grid model	29

Fig 17. Two very non-uniform floor plans	29
Fig 18. Radio statistics comparisons for two very non-uniform floor plans	30
Fig 19. Percentage of tail area of PDF as a function of number of antennae for different thresholds	31
Fig 20. Radio map locations where power is 35 dB below maximum	31
Fig 21. 2-D spatial autocorrelation of deep-fade pattern for a 30m by 30m	32
Fig 22. Empty-cell mode	39
Fig 23. Two limiting cases of the RF statistical distribution in the "empty cell" model	41
Fig 24. Model with wall grids. (Paths 1 and 2)	42
Fig 25. Illustration of image antenna distribution	44
Fig 26. Radio statistics comparisons for different R and T	46
Fig 27. Radio statistics comparisons for different d , R , and T	47
Fig 28. Radio statistics for different antenna numbers	48

ABSTRACT OF FINAL REPORT

During the course of this research contract, we have concentrated on the device and system aspect of distributed antenna systems aimed towards support wireless communications in an in-building environment. The infrastructure is fiber-based, but with the key criterion being low-cost. As such, we address the issue both from the device end and from the system end. From the device end, we investigated VCSELS as optical sources for the fiber-optic network, since VCSELS are the lowest cost of ANY active transmitter component available to date, and projected to continue into the future. In particular, we investigated VCSELS novel structures in which a voltage biased quantum well absorber is embedded in the mirror stack. The added RF functionalities lead to several applications for these devices were demonstrated.

From the systems end, we have examined network architectures which lead to the lowest cost solution. The architecture we developed is called a "saturated" antenna architecture. This approach offers the possibility of negating the need for site-specific planning, modeling and survey for deployment of in-building wireless systems, and is possible only with RF photonics hardware of sufficiently low cost, such as those offered by VCSEL transmitter systems. We investigate the characteristic radio distribution statistics under this scenario, and found that with a "sufficiently large" number of antennae elements per unit area, the radio statistics approaches certain limiting distributions which are largely independent of the specific floor-plan. These limiting distributions can be accurately predicted, **without invoking adjustable parameters**, using only a few key "global" building parameters which can be easily determined for a given building. A system of this type can thus be rapidly and inexpensively deployed.

Section 1 of this report describes in detail the design and RF characteristics of quantum-well absorber-embedded VCSELS, and the RF photonic applications made possible by this novel device. Section 2 describes the basic "saturated" antenna architecture approach, and extensive simulation results justifying the high performance of this approach. Section 3 approaches the "saturated" antenna architecture analytically, and arrives at a fundamental understanding of the mechanism on which the saturated antenna network operates, and factors which leads to the results we observed in the simulation. This approach leads to a solid understanding of the performance of such a network and its dependence on various parameters of the system.

1. RF photonics by VCSELS with embedded quantum-well absorber

Section Abstract

A VCSEL with an embedded quantum-well absorber exhibits very interesting and useful RF properties. The underpinning of these properties are regimes of negative differential resistance in the absorber under varying laser bias conditions. By choosing the absorber bias conditions such that the operating load line intersects the absorber IV trace three times, the laser can be made to exhibit optical bistability. The magnitude of the bistability and consequent hysteresis loop can be controlled by adjusting the absorber bias. If the bias conditions are adjusted so that the load line is tangential to the portion of the absorber I-V exhibiting negative differential resistance, then the device can be made to self-pulsate. Self-pulsations at frequencies as high as 2 GHz with 700 kHz RF linewidth FWHM (full-width at half-maximum) have been obtained using these devices. Furthermore, the self-pulsation frequency can be tuned over 700 MHz by adjusting the bias conditions, representing a substantial advance over existing self-pulsating VCSELS.

We have also demonstrated a novel modulation scheme using these devices, in which the drive signal is applied to the bias voltage across the absorber. Theoretical analysis of the chirping mechanism leads us to expect that this technique will minimize the chirp at high modulation frequencies, while still providing substantial modulation depth and high speeds. We achieved a -3 dB bandwidth of 9 GHz; the bandwidth increases with the laser bias current at a rate of 7 GHz/mA^{1/2}.

1.1 Introduction

We have constructed a novel vertical-cavity surface-emitting laser (VCSEL) with a quantum-well absorber integrated into the mirror stack. The absorption can be varied by applying a voltage bias across the absorber junction, which effectively changes the mirror reflectivity and hence varies the laser output power. We have demonstrated several applications for this new device, including optical bistability, self-pulsation, and a novel intracavity absorber modulation scheme.

Self-pulsating lasers have found extensive commercial use in applications such as optical disk readout and multimode fiber communications networks because the extremely short coherence length of self-pulsating lasers renders them relatively insensitive to optical feedback. Although

self-pulsation has been demonstrated previously in edge-emitting lasers which use integrated active saturable absorbers to obtain controllable self-pulsations up to GHz frequencies, recent work has focused on obtaining self-pulsating VCSELs.[1-3] The surface-normal geometry of VCSELs leads to advantages such as circular beam output and the potential for two-dimensional arrays. Initial demonstrations of self-pulsating VCSELs used defects caused by ion implantation as passive saturable absorbers; these efforts produced at most MHz-range pulsations with RF linewidths of roughly 100 MHz.[4] Using our new VCSEL, which has an active quantum-well absorber integrated into the mirror stack, we obtain reproducible self-pulsations with repetition rates of greater than 2 GHz and RF linewidths of 700 kHz.[5,6] Furthermore, we demonstrate tuning of the self-pulsation frequency over 700 MHz. In this section, we present the experimental results and discuss in detail the mechanism which yields optical bistability and self-pulsation in these devices.

We also use this structure to demonstrate a novel modulation technique in which the modulation signal is applied directly to the intracavity quantum-well absorber. Ideally, a VCSEL modulation scheme should provide a high modulation depth and low frequency chirp, while still being high-speed. Although direct current modulation has been demonstrated at high speeds and for large modulation depths, changing the carrier density results in frequency chirp, limiting both digital and large-signal AM applications.[7-9] Frequency chirp can be avoided by using an external modulator; however, the extinction ratio obtained using this technique is low and insertion loss is problematic. As an alternative, we demonstrate a scheme in which the modulation is applied to a quantum-well absorber integrated *within* the VCSEL mirror stack.[10-11] Modulating the absorber causes the mirror reflectivity to vary, resulting in modulation of the laser output power. We expect the modulation bandwidth using this technique to be comparable to that of direct current modulation. The device can also be designed for high modulation depth by positioning the modulator quantum-well absorption edge to be slightly shorter than the Fabry-Perot wavelength, so that as the absorption edge red-shifts with increasing applied reverse bias it is swept across the Fabry-Perot wavelength. The placement of the absorber at a peak of the internal optical field intensity distribution results in high modulation efficiency. Furthermore, we analyze the modulation chirp properties and show that our technique should lead to significantly less frequency chirp than does direct modulation at high frequencies. Using intracavity absorber modulation, we demonstrate a 3-dB bandwidth of 9 GHz and a modulation efficiency of 7 GHz/ $\sqrt{\text{mA}}$. These

results are limited only by the relaxation oscillation frequency and could be increased substantially by implementing the design improvements suggested below.

1.2 Device Structure

The device, which is shown in Figure 1a, is a VCSEL with an n-p-n configuration. The bottom p-n junction is used to forward bias a two or three quantum-well gain region. The top n-p junction allows reverse biasing of a single quantum-well absorber positioned in the top mirror stack as shown. Current and modal confinement are achieved using two oxide layers. This device is similar to that of an integrated VCSEL detector in Reference 12, where details of design and fabrication can be found.[12]

The electronic driving circuit used with the device varies depending on the desired application. To obtain optical bistability or self-pulsation of the device, the bias circuit shown in Figure 1b is used. The absorber is biased using a variable resistor R in series with a voltage source V_0 . A 50Ω termination path is provided for any AC current generated in the absorber, and the gain section is biased with a DC current source. The driving circuit used to perform high speed absorber modulation is shown in Figure 1c. In this case, the absorber is reverse biased with a DC voltage source, and the AC modulation signal is superimposed using a bias-T. The p-contact of the device serves as the common ground for both the absorber and the active regions. A DC current source is used to pump the active region, while a $50\text{-}\Omega$ termination path is provided for any AC signal generated in the gain region.

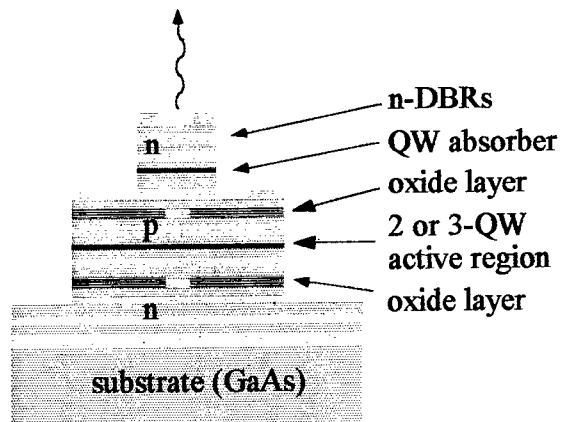


Figure 1a. Device schematic

Figure 1b. Electronic bias circuit for optical bistability and self-pulsation.

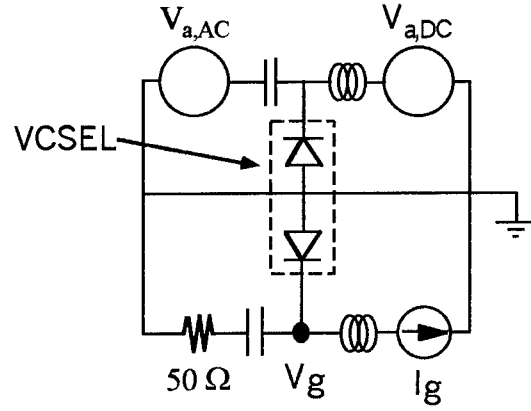
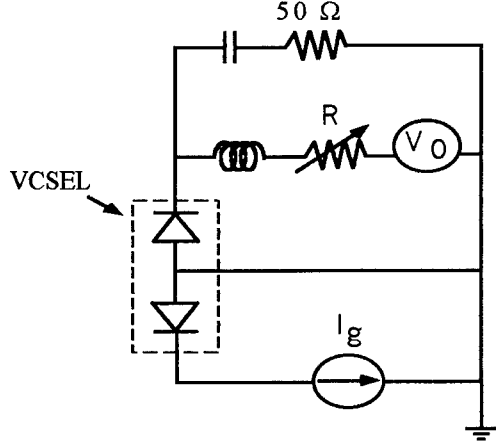


Figure 1c. Electronic bias circuit for absorber modulation.

1.3 Negative Differential Resistance

The longitudinal modes of this device are very widely spaced due to the characteristic short cavity length of a VCSEL. Thus, the lasing wavelength of the device at a fixed bias current is determined by the Fabry-Perot wavelength, providing a design flexibility which is not available in edge-emitting devices. This flexibility, which is discussed in Reference 6, allows us to obtain a large negative differential resistance in the absorber using small absorber bias voltages and potentially at high laser powers[6].

To illustrate this effect, we engineered two VCSELs, with differing placements of the lasing wavelength relative to the absorption wavelength, defined by the peak of the absorption spectrum when no bias voltage is applied to the absorber. In Device A, the absorption wavelength, which is designed to be 851nm, is 23nm longer than the lasing wavelength of 828nm. The gain region of this device is composed of three 70Å $\text{In}_{0.2}\text{Ga}_{0.8}\text{As}$ quantum-wells and is designed to be centered at 843nm. The single quantum-well absorber is 90Å thick, with the current-voltage (I_a - V_a) characteristic shown in Figure 2a. In Device A, the I_a - V_a response shifts downwards with increasing laser power, so the absorber behaves like a typical photodiode.

In contrast, Device B is designed so that the absorption wavelength (approximately 940nm) is 26nm shorter than the lasing wavelength (966nm). The gain region centered at 940nm is comprised of two 80Å quantum-wells, and the absorber quantum well is also 80Å thick. The absorber I_a - V_a characteristic for Device B exhibits a regime of negative differential resistance, as shown in Figure 2b. Figure 3 illustrates the origin of this regime. For a constant DC gain bias current, the lasing wavelength is fixed. When a voltage bias is applied to the absorber, the absorption spectrum redshifts and broadens due to the quantum confined Stark effect, effectively sweeping the absorption peak across the lasing wavelength as shown in Figure 3a. This causes a region of negative differential resistance in the absorber I_a - V_a response; see Figure 3b. Typically, an absorber bias voltage (V_a) of about 1.5V is required to obtain the negative differential resistance. This bias voltage is applied across the $5\lambda/4$ (300nm) intrinsic region, so the applied field is about 5×10^4 V/cm.

Furthermore, the lasing wavelength redshifts with applied laser bias, altering its position relative to the absorption wavelength. This observation suggests the potential to obtain high power operation of our device by positioning the Fabry-Perot wavelength slightly closer to the absorption peak.

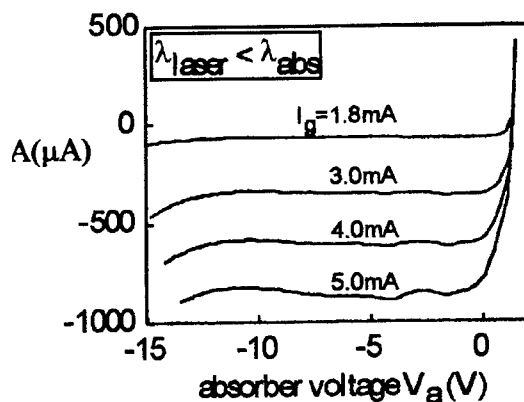


Figure 2a. Absorber current vs. voltage (I_a - V_a) traces for Device A, with varying laser bias current I_g . For this device, the absorption wavelength is 23nm longer than the lasing wavelength.

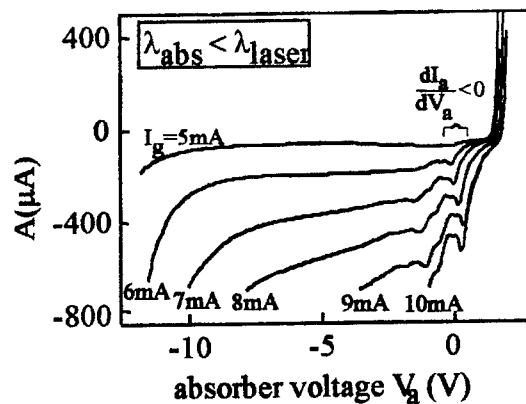


Figure 2b. Absorber current vs. voltage (I_a - V_a) traces for Device B, with varying laser bias current I_g . For this device, the absorption wavelength is 26nm shorter than the lasing wavelength. The I_a - V_a traces exhibit a regime of sharply negative differential resistance (NDR).

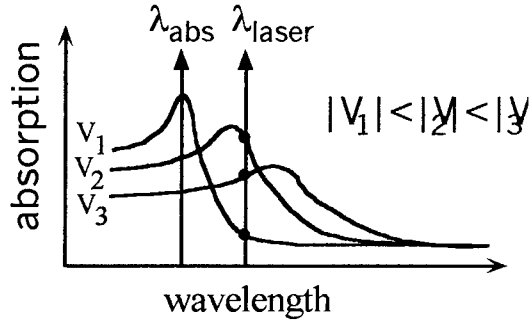


Figure 3a. Origin of the sharp region of negative differential resistance in the absorber I-V trace. The absorption spectrum redshifts with applied voltage bias, sweeping the absorption peak across the lasing wavelength.

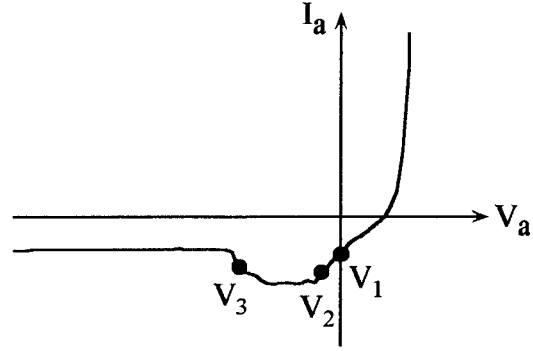


Figure 3b. The absorber IV trace resulting from the sweeping of the absorption peak in Fig 3a displays negative differential resistance.

1.4 Optical Bistability

We exploit the negative differential resistance exhibited by the absorber I_a - V_a traces of Device B in order to obtain either optical bistability or self-pulsation. For these applications, Device B is electronically biased as shown in Figure 1b. Our work on optical bistability is presented in Reference 5.[5]

The device can be operated in a bistable manner by choosing the absorber bias (R and V_0) such that the operating load line intersects a single absorber I_a - V_a trace three times, as shown in Figure 4a.[3,5] Power-current (L - I_g) traces of a typical Device B, with the absorber biased so that the load line intersects the absorber I_a - V_a trace three times, are shown in Figure 4b. A noticeable discontinuity in dL/dI_g and a hysteresis loop occur at threshold, indicating bistable operation. Figure 4b shows that the hysteresis loop can be closed by decreasing the absorber bias resistance R .

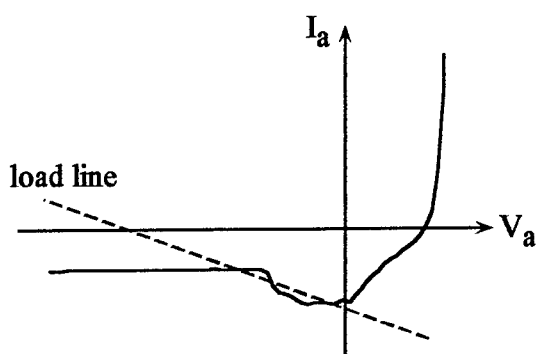


Figure 4a. Bistable operation: the absorber is biased so that the operating load line intersects the absorber I_a - V_a trace three times.

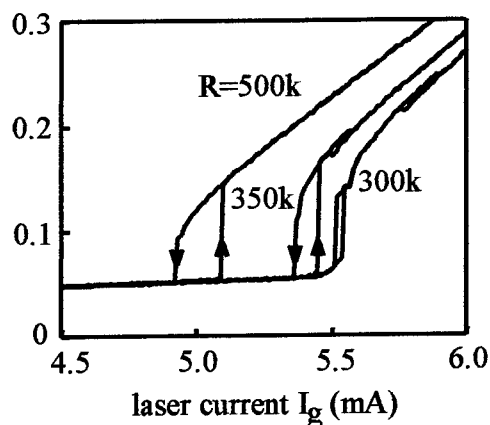


Figure 4b. Bistable operation: the L - I_g trace exhibits a discontinuity in dL/dI_g and a hysteresis loop. Absorber is biased with $V_0=40V$ and $R=500k\Omega$, $350k\Omega$, or $300k\Omega$.

1.5 Self-pulsation

Self-pulsation of Device B is achieved by adjusting the absorber bias conditions so that the operating load line is tangential to the region of negative differential resistance in the absorber I_a - V_a trace; see Figure 5a. Because Device B is designed as discussed in Section 3 to obtain regions of sharp negative differential resistance in the absorber I_a - V_a characteristic, relatively low absorber biases ($R=10$ - $100k\Omega$, $V_0=5$ - $15V$) are required to obtain self-pulsation. A complete discussion of our work on obtaining self-pulsation is given in References 5 and 6.[5,6]

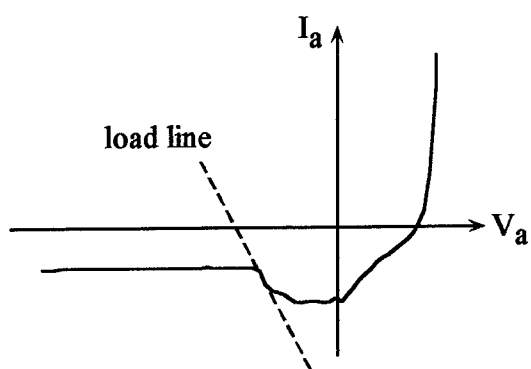


Figure 5a. Self-pulsation regime: the absorber is biased so that the operating load line is tangential to the absorber I_a - V_a trace.

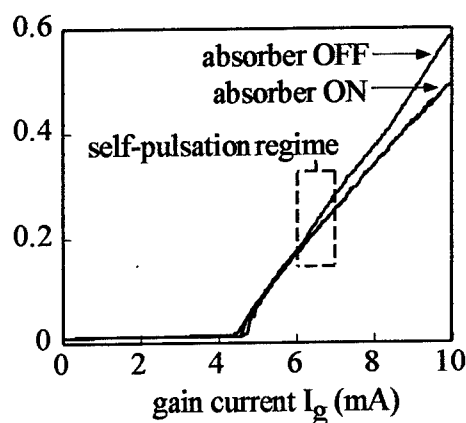


Figure 5b. Self-pulsation regime: the L - I_g trace.

Typical power versus current ($L-I_g$) traces are shown in Figure 5b both for the case in which the absorber bias is turned off ($R=0$, $V_0=0$), so that the device operates as a standard VCSEL, and also for the case in which the absorber is biased appropriately for self-pulsation. As expected, when the absorber bias is turned on, the lasing threshold of the device increases. For the particular absorber bias (R , V_0) used, the $L-I_g$ curve exhibits a sharp jump and a narrow hysteresis loop near threshold. We observe self-pulsation of the device when the laser bias current is about 1.5 times the threshold current, as indicated by the boxed region in Figure 5b. The jump in the $L-I_g$ curve indicates that just above threshold the device is operating in a bistable manner because the operating load line thrice intersects the absorber I_a-V_a trace when the gain bias current $I_g=5\text{mA}$. When the gain current $I_g=6-7\text{mA}$, which is the necessary condition for self-pulsation with the given absorber bias conditions ($R=75\text{k}\Omega$, $V_0=7\text{V}$), the load line is tangential to the absorber I_a-V_a response. In practice, self-pulsation of the device can be obtained at a range of bias currents (I_g) and output powers by choosing R and V_0 so that the load line is tangential to the absorber I_a-V_a trace at the desired bias current. This unique feature arises due to the ability to control the laser and absorber wavelengths independently, representing a major design strength of our device.

We measure the output of the device using an RF spectrum analyzer. When the device is biased so that it does not self-pulsate, the RF spectrum shows only a broad peak due to relative intensity noise; see Figure 6a. When the absorber bias conditions are adjusted such that the operating load line is tangential to the region of negative differential resistance in the absorber IV, the device self-pulsates at a GHz-range repetition rate, resulting in the sharp peak in the RF spectrum shown in Figure 6b. The self-pulsation peak is roughly 40dB above background, and has an extremely narrow RF linewidth of 700 kHz, as illustrated by the enlarged RF trace shown in Figure 6c.

The observed self-pulsations occur at a repetition rate equal to the relaxation oscillation frequency of the device. Hence, the self-pulsation frequency can be tuned by varying the DC gain bias current. As the gain bias current is varied, the absorber bias (R and V_0) must be adjusted so that the operating load line remains tangential to the absorber IV in order to maintain self-pulsation. Figure 7 shows that the pulsation frequency obeys a square root dependence on the gain bias above threshold, as expected. We demonstrate tuning of the self-pulsation frequency over 700 MHz using this technique.

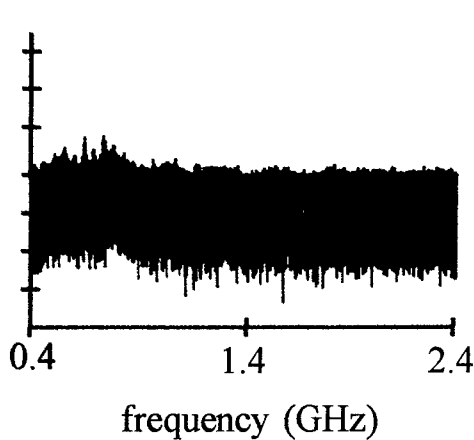


Figure 6a. Self-Pulsation OFF: RF Spectrum Analyzer trace of the device output when the absorber is not biased for self pulsation ($R=100k\Omega$, $V_0=10V$, $I_g=5.3mA$).

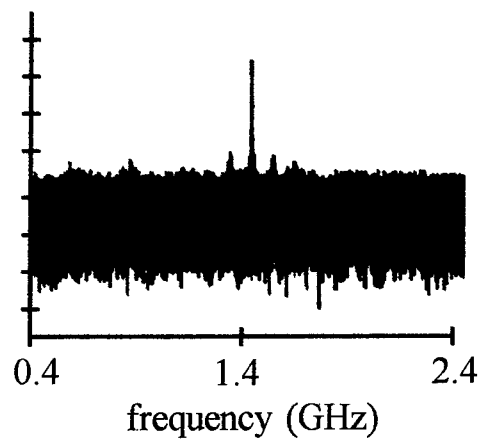


Figure 6b. Self-Pulsation ON: RF Spectrum Analyzer trace of the device output when the absorber is biased for self pulsation ($R=75k\Omega$, $V_0=7V$, $I_g=6mA$).

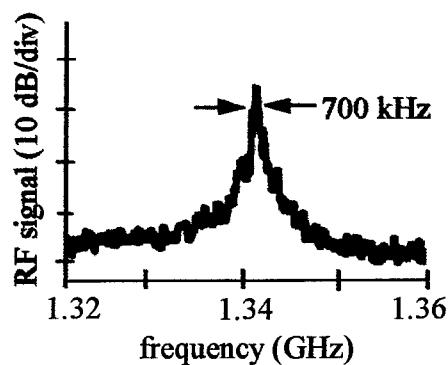


Figure 6c. Self-Pulsation ON: RF Spectrum enlarged to show RF linewidth of self-pulsation peak.

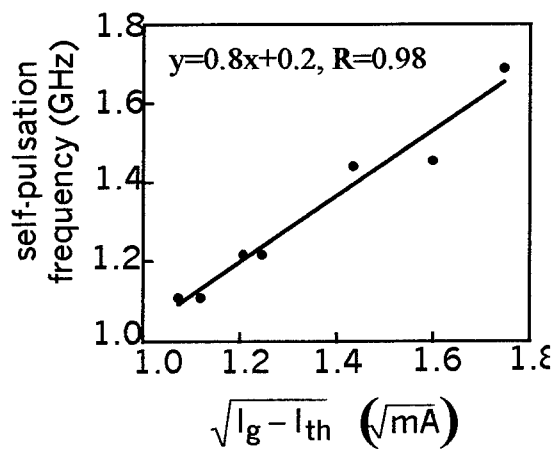


Figure 7. Tuning of the self-pulsation frequency by adjusting the gain bias current I_g .

1.6 absorber modulation

1.6.1 Experimental Results

We demonstrate high-speed modulation of the intracavity absorber using a device of Type A (see Figure 2a above). This work is described in References 10 and 11.[10,11] The 828nm lasing wavelength of Device A is 23nm shorter than the absorption wavelength, which is designed to be 851nm. The electronic driving circuit used for these measurements is shown in Figure 1c.

The $L-I_g$ and V_g-I_g characteristics of a typical Device A are shown in Fig. 8. The threshold current is 1.7 mA, and the threshold voltage is 5.6 V. The output power typically peaks at 0.7 mW.

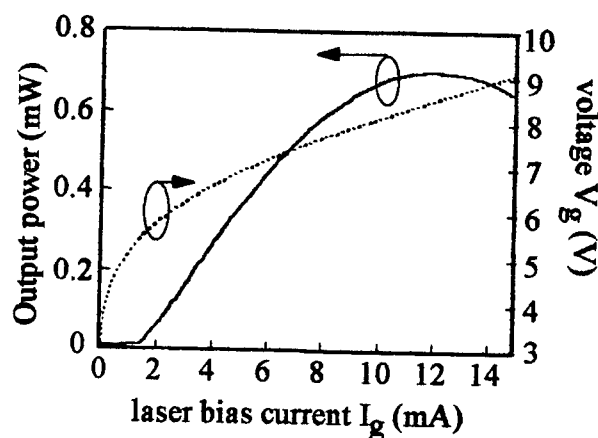


Figure 8. $L-I_g$ and V_g-I_g for a typical Device A with the absorber voltage $V_a=0$.

Figure 9a shows the response of the device to absorber modulation under several DC bias conditions (I_g) for the gain region. The experimental results indicate a -3-dB bandwidth of 9 GHz at $I_g = 8$ mA. The bandwidth as well as the relaxation oscillation frequency increase with laser bias current I_g as expected in conventional modulation; see Figure 9b. We achieved 7 GHz/ $\sqrt{\text{mA}}$ in the linear regime, rolling off to 1.7 GHz/ $\sqrt{\text{mA}}$.

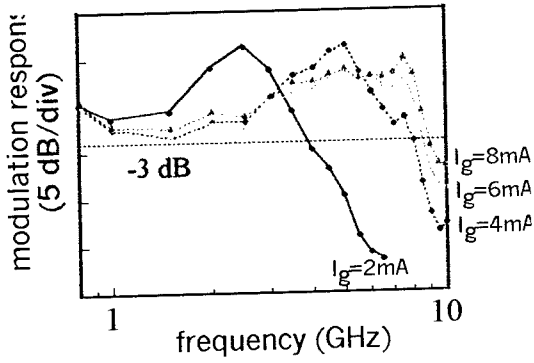


Figure 9a. Absorber modulation response for fixed DC absorber bias ($V_{a,DC} = -1V$) and varying laser bias current

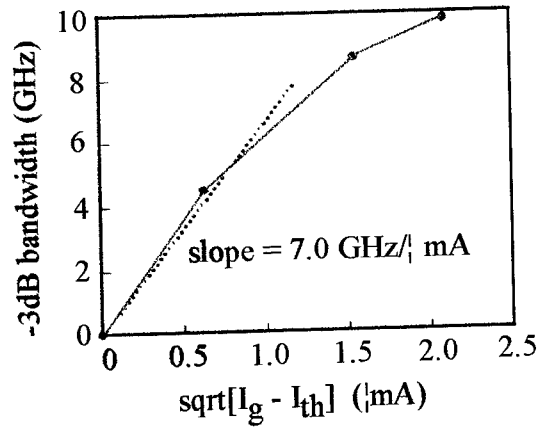


Figure 9b. $L-I_g$ and V_g-I_g for a typical Device A with the absorber voltage $V_a = 0$.

We also measured the absorber modulation response for fixed laser bias currents and at different DC absorber biases. The results in Figure 10 indicate that the bandwidth does not change appreciably with varying absorber DC bias.

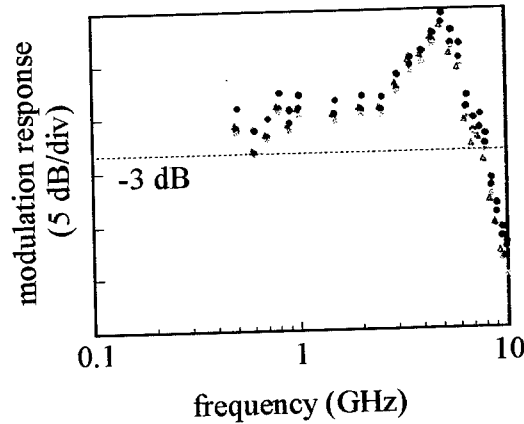


Figure 10. Absorber modulation response for fixed gain bias current I_g and varying DC absorber bias ($V_{a,DC} = 0V, -1V, -3V, -4V$).

1.6.2 Discussion of Frequency Chirp

The frequency chirp due to intracavity absorber modulation is compared in the following discussion and in Reference 11 to the chirp introduced by conventional direct current modulation.[11] Modulating the absorber effectively modulates the mirror loss since the absorber is part of the VCSEL mirror stack. This in turn leads to modulation of the photon lifetime.

We compare the frequency chirp due to intracavity absorber modulation ($\delta\tau_p$, where τ_p is the photon lifetime) to the chirp obtained using direct current modulation (δJ , where J is the injected current density) by performing a small-signal analysis of the rate equations. Define δn_y to be the change in the carrier density of the gain region when the absorber is modulated (i.e. $\delta J = 0$). Likewise, define δn_J to be the change in the carrier density of the gain region when the pump current is modulated (i.e. $\delta\tau_p = 0$). The ratio of the two, $|\delta n_y / \delta n_J|$, provides a comparison of the chirp produced by the two techniques. Note that this ratio depends on the modulation frequency ω :

$$\frac{\delta n_y}{\delta n_J} = - \frac{\left(v_g g + S v_g \frac{\partial g}{\partial S} \right) \left(S v_g \Gamma \frac{\partial g}{\partial n} + 2 \Gamma \beta_{sp} B n \right)}{\left(i\omega + \frac{1}{\tau_{\Delta e}} + S v_g \frac{\partial g}{\partial n} \right) \left(i\omega - \Gamma v_g g + \frac{1}{\tau_p} - S v_g \Gamma \frac{\partial g}{\partial S} \right)} \quad (1)$$

where v_g = group velocity, S = photon density, g = gain, Γ = confinement factor, β_{sp} = spontaneous emission factor, $\tau_{\Delta e} = (A + 2Bn + 3Cn^2)^{-1}$, A = nonradiative recombination coefficient, B = radiative recombination coefficient, and C = Auger recombination coefficient.

The magnitude of the two-pole response given by (1) monotonically decreases with ω due to the heavy damping introduced by $\partial g / \partial S$ and $\partial g / \partial n$. For frequencies greater than f_c (the frequency at which $|\delta n_y / \delta n_J| = 1$), absorber modulation produces less chirp than direct modulation. From equation (1):

$$\begin{aligned} \omega_c = 2\pi f_c &\approx \sqrt{S v_g \Gamma \frac{\partial g}{\partial n} \left(v_g g + S v_g \frac{\partial g}{\partial S} \right)} \\ &\approx \sqrt{\omega_R^2 + S^2 v_g^2 \Gamma \frac{\partial g}{\partial n} \cdot \frac{\partial g}{\partial S}} \end{aligned}$$

where ω_R is the resonance frequency. Since $\partial g / \partial S$ is negative, f_c is less than the resonance frequency. Figure 11 shows the calculated effect of absorber and gain modulation on the carrier

density in the gain region for the same photon modulation depth and standard VCSEL parameters. From Fig. 13, the ratio of the -3dB-frequency f_{-3dB} to f_C is 1.6, so the critical frequency occurs well within the useful bandwidth of the device. Hence, absorber modulation at frequencies between f_C and f_{-3dB} results in less chirp than does direct gain modulation. The carrier density within the absorber layer is also modulated. However, the absorber is far away from the active region, so any frequency chirping effects should be quite small.

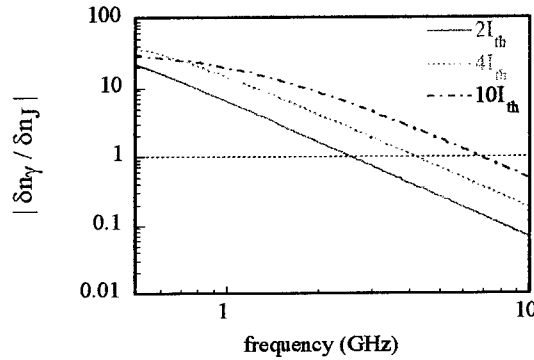


Figure 11. Predicted effect of absorber and direct modulation on carrier density in the gain region. When $|\delta n_g| < |\delta n_f|$, absorber modulation results in less chirp than does direct gain modulation.

1.6.3 Design Criteria

The relative placement of the gain peak wavelength (λ_{gain}), the absorption peak wavelength (λ_{abs}), and the Fabry-Perot transmission peak wavelength (λ_{FP}) is an important design criterion for this device. Ideally, we should have $\lambda_{gain} < \lambda_{FP}$ in order to achieve maximum overlap of the gain peak with the Fabry-Perot as the gain peak red-shifts with increasing pump current. Furthermore, we desire that $\lambda_{abs} < \lambda_{FP}$ with these two wavelengths fairly close to each other, so that a small change in the applied voltage across the absorber induces a large change in the absorption due to the quantum-confined Stark effect. Since the wavelength of the pumped gain region will shift further than will the wavelength of the voltage-biased absorber, the ideal relative positioning of the three wavelengths should be $\lambda_{gain} < \lambda_{abs} < \lambda_{FP}$.

Next consider what happens when the ideal conditions are not met. Placing the Fabry-Perot wavelength too much longer than the peak wavelength of the gain or absorber leads to poor modulation efficiency, as shown in Reference 14, since greater voltages across the absorber are required to sweep the absorption edge across the Fabry-Perot wavelength.[14] Furthermore, the smaller overlap of the gain peak with the Fabry-Perot results in a narrow bandwidth, also evident in Reference 14.

In the device used for the experimental measurements discussed in Section 6.1, the Fabry-Perot wavelength (828 nm) is shorter than that of the gain (~ 843 nm) or absorber quantum well (~ 851 nm). In this case, changing the absorber DC bias does not result in a significant change in the absorption or the modulation response, as shown in Figure 10.

We expect that aligning the Fabry-Perot wavelength to be redder than the absorber quantum-well band edge will result in excellent modulation depth with this absorber modulation technique. A reverse bias across the absorber can then be used to sweep the absorption edge across the laser emission, resulting in a very high on-off ratio. Future work will include optimization of the bandwidth, growth and fabrication for large-signal modulation, and single-mode operation to demonstrate low frequency chirp.

1.7. Conclusions

In conclusion, we have constructed a novel VCSEL with a voltage-controlled, quantum-well absorber integrated into the mirror stack. If the device is designed so that the absorber wavelength is slightly shorter than the Fabry-Perot wavelength under no applied bias, the device exhibits a region of sharp negative differential resistance in the absorber current versus voltage characteristic. By choosing the absorber bias conditions so that the operating load line either thrice intersects or is tangential to the absorber I_a - V_a trace, the device can be made to exhibit either optical bistability or self-pulsation, respectively.

Using this device, we produced for the first time tunable self-pulsations with an extremely narrow RF linewidth of 700 kHz. By simply adjusting the bias conditions, the GHz-range self-pulsation

frequency can be tuned over 700 MHz. By careful device design, the VCSEL can be made to self-pulsate at low absorber biases, GHz-range frequencies, and potentially at high output power.

Alternatively, the device can be designed with the lasing wavelength slightly shorter than the absorber wavelength. Using this device design, we have demonstrated a novel technique of intracavity quantum-well absorber modulation of a VCSEL. We achieved with this method reasonable small-signal bandwidths of 9 GHz and a bandwidth dependence on pump current of 7 GHz/ $\sqrt{\text{mA}}$. We analyzed the chirp of an intracavity modulator in comparison with that of direct modulation and showed significantly less chirp in our technique at higher frequencies. Future work will include optimization of the bandwidth, growth and fabrication for large-signal modulation, and single-mode operation to demonstrate low frequency chirp.

1.8. Section Reference

- [1] P. J. Anthony, T. L. Paoli, and Robert L. Hartman, "Observations of Negative Resistance Associated with Superlinear Emission Characteristics of (Al,Ga)As Double-Heterostructure Lasers," *IEEE Journal of Quantum Electronics*, **16** (7), p. 735-739, 1980.
- [2] J. P. van der Ziel, "Time-dependent voltage measurement of pulsating $\text{Al}_x\text{Ga}_{1-x}$ double-heterostructure lasers," *Applied Physics Letters*, **35** (2), p. 116-118, 1979.
- [3] Ch. Harder, K. Y. Lau, and A. Yariv, "Bistability and pulsations in semiconductor lasers with inhomogeneous current injection," *IEEE Journal of Quantum Electronics*, **18** (9), p. 1351-1361, 1982.
- [4] X. Tang, J.P. van der Ziel, B. Chang, R Johnson, and J.A. Tatum, "Observation of bistability in GaAs quantum-well vertical-cavity surface-emitting lasers," *IEEE Journal of Quantum Electronics*, **33** (6), p. 927-932, 1997.
- [5] S. F. Lim, J. A. Hudgings, G. S. Li, W. Yuen, K. Y. Lau, and C. J. Chang-Hasnain, "Self-pulsating and bistable VCSEL with controllable quantum-well saturable absorber," *Electronics Letters*, **33** (20), p. 1708-9, 1997.
- [6] J. A. Hudgings, S. F. Lim, G. S. Li, W. Yuen, K. Y. Lau, and C. J. Chang-Hasnain, "Self-pulsating VCSEL with a Voltage-Controllable Pulsation Frequency," submitted to *IEEE Photonics Technology Letters*, 1997.

- [7] K. L. Lear, V. M. Hietala, H. Q. Hou, J. Banas, B. E. Hammons, J. Zolper, and S. P. Kilcoyne, presented at *Conference on Lasers and Electro-Optics (CLEO'97)*, Baltimore, MD, 1997.
- [8] J. W. Scott, B. J. Thibeault, C. J. Mahon, and L. A. Coldren, *Applied Physics Letters*, **65** (12), p. 1483-1485, 1994.
- [9] F. S. Choa, Y. H. Lee, T. L. Koch, C. A. Burrus, B. Tell, J. L. Jewell, and R. E. Leibenguth, *IEEE Photonics Technology Letters*, **3** (8), p. 697-699, 1991.
- [10] S. F. Lim, J.A. Hudgings, L.P. Chen, G. S. Li, W. Yuen, K.Y. Lau, and C. J. Chang-Hasnain, "Modulation of a vertical-cavity surface-emitting laser using an intracavity quantum-well absorber," accepted for publication in *IEEE Photonics Technology Letters*, 1997.
- [11] S. F. Lim, J.A. Hudgings, L.P. Chen, G. S. Li, W. Yuen, K.Y. Lau, and C. J. Chang-Hasnain, "Novel intracavity modulator integrated with a vertical-cavity surface-emitting laser," in *Trends in Optics and Photonics Series (TOPS)*, C.J. Chang-Hasnain, Ed., Washington, D.C., Optical Society of America, vol. 15., pp.48-52, 1997.
- [12] S. F. Lim, G. S. Li, W. Yuen, and C. J. Chang-Hasnain, " Vertical-Cavity Lasers with an Intracavity Resonant Detector," *IEEE Selected Topics in Quantum Electronics*, April 1997, **3** (2), p. 416-21.
- [13] J. Palaski and K. Y. Lau, "Parameter ranges for ultrahigh frequency mode locking of semiconductor lasers," *Applied Physics Letters*, **59** (1), p. 7-9, 1991.
- [14] S. F. Lim, L. P. Chen, G. S. Li, W. Yuen, K. Y. Lau, and C. J. Chang-Hasnain, presented at *Conference on Lasers and Electro-Optics (CLEO'97)*, Baltimore, MD, 1997.

2. In-building Radio Distribution Using a "Saturated" Distributed-Antenna Architecture

Section abstract

The radio-propagation environment inside buildings is of sufficient complexity such that the design of an in-building wireless communication system often necessitates site-specific radio planning/modeling/measurements. A distributed-antenna architecture is often employed for in-building radio distribution. Sophisticated simulation tools have been developed to determine the proper placement of the antennae. With the recent emergence of very low cost distributed-antenna hardware, it becomes economically feasible to blanket a building with a large number of antennae elements (the "saturating approach"). This offers the possibility of negating the need for site-specific planning, modeling and survey for deployment of in-building wireless systems. We investigate the characteristic radio distribution statistics under this scenario, and found that with a "sufficiently large" number of antennae elements per unit area, the radio statistics approaches certain limiting distributions which are largely independent of the specific floor-plan. These limiting distributions can be accurately predicted, **without invoking adjustable parameters**, using only a few key "global" building parameters which can be easily determined for a given building. Quantitative results from simulation, as well as what constitutes a "sufficiently large" number of antenna elements, are described in detail in this section.

2.1 Introduction

The next generation of wireless radio systems promises to give consumers the luxury of tether-less access to telephone conversation, email, and network services. It is clear that to meet the demand of these new services, cellular and PCS service providers must upgrade their networks to provide complete radio coverage, both outdoor and indoor. Outdoor wireless coverage is currently provided by macrocellular base-stations, supplemented by coaxial or fiber-optic analog transport links (the *wired* RF transport infrastructure) which distribute the RF signal to areas of poor coverage such as subway tunnels, shopping malls and shadowed regions[1-3]. In addition to providing a more uniform radio coverage, this type of "distributed-antenna" network can be used to optimize radio channel utilization by dynamically allocating channel resources according to local

traffic pattern throughout the course of the day.

The concept of applying distributed-antenna architecture to in-building radio distribution has been proposed and discussed in considerable detail[4,5]. For practical deployment, it is necessary to address the following issues. First, the fiber-optic and coaxial cable links used for outdoor coverage are high performance, high dynamic-range systems and thus are expensive, therefore it is not economically feasible to deploy a large number of such links and antennae inside a typical office building. On the other hand, the in-building radio propagation environment is a very complex one, necessitating radio-modeling/planning using sophisticated simulation tools, and/or site survey, in order to decide on the proper locations of the antennae. This is exacerbated by the high cost of installing single-mode fibers and heavy coaxial cables in odd locations inside buildings (as dictated by radio propagation requirements) where there are no existing conduits or cable troughs. All these issues combined, raises substantial obstacles and challenges for realizing truly ubiquitous and seamless wireless coverage of the next-generation cellular networks.

2.2. "Saturated" distributed-antenna architecture

Instead of minimizing the number of antenna deployed in a building to reduce cost, we propose a contrary paradigm of using a *large number* of antennae for in-building coverage. This becomes practically feasible with the recent availability of very-low cost distributed-antenna hardware[6]. We argue that this approach will *minimize* the **total** cost of deploying the system instead of increasing it, as follow:

1. The overall radio power distribution inside the building becomes more uniform as the density of antenna is increased, thus reducing the dynamic range requirements of both the individual antenna units, and the analog cable links that interconnect them. (Another way to state this is that as the area covered by each antenna is reduced, the performance requirements are correspondingly reduced.) This translates into a cost reduction in hardware, particularly since single-mode fibers and heavy coaxial cables are no longer needed in order to meet the stringent RF transport requirements otherwise.
2. While detailed radio planning is needed to cover a building with a small number of antennae due to large variations between building structures and floor plans, we found that the radio distribution becomes independent of the exact floor plan and the placement of the antennae,

when a "large" number of antenna is deployed. Under this circumstances, we found it suffice to specify only a few global parameters that characterize the building whereby the radio distribution statistics of the entire building can then be predicted with a high level of confidence. We will substantiate this assertion in the sections to follow. This constitutes the bulk of the content of this section.

3. Under this scenario, there should be no need to perform detailed radio modeling or planning in order to deploy an in-building distributed-antenna system. The global building parameters yields the global radio statistics and the dynamic range performance required of the radio hardware, as well as the number of antennae needed; deployment of the antennae and the wired RF transport infrastructure can be carried out in existing building conduits and cable troughs since the exact locations of the antennae now becomes non-critical, the ease of deployment and the reduced hardware requirements contribute to reduced installation cost for the whole system.

2.3 In-building radio modeling and simulation

Previous work on in-building radio modeling involved, in one approach, establishing a power-decay law of the path loss whereby the relation between the power-decay exponent and the general building type is established by experimental measurements[7,8]. The radio power at a given point in the building is determined simply by measuring its distance to an antenna. For a distributed-antenna system, one simply sums the radio powers emitted by the multiple antennae using the power-decay law. An improved version of this approach includes wall attenuation by counting the number of walls separating the point of observation and the antennae sources. Fading statistics due to multiple antenna sources or reflection from walls are not taken into account, which can be a serious deficiency in modeling a distributed-antenna system. A second approach uses ray-tracing simulation algorithm to predict the radio distribution based on the building floor plan, which includes such detailed information as locations and reflection properties of all walls and partitions[9-11]. These approaches are deterministic and are appropriate to studying site-specific radio propagation effects in a given building served by a small number of antennae, of which the detailed floor plan and radio characteristics of building materials are known to a high degree of certainty. Sophisticated simulation tools have already been developed for performing these planning

tasks.

An alternative approach is to deal with the radio coverage problem on a statistical basis. Instead of attempting to predict the radio power at a specific point in space inside the building, the statistics over the entire building is expressed as a distribution, from which the global performance of the wireless communication system such as dynamic range requirements and call-blocking probability, etc., can be predicted. It is a useful approach, particular since intense computation is not required as in ray-tracing approach, but only if such radio statistical distributions can be predicted with sufficient accuracy. These statistical distributions are commonly derived based on ideal models of physical processes (such as addition of random vectors of equal magnitudes for Rayleigh distribution, that with a dominant component for Rician, and others such as Nakagami, etc., [12-16]). As in the power-decay law approach, these ideal physical models are too simplistic to incorporate actual building parameters in a meaningful way, and as such does not really provide an alternative to detailed ray-tracing for actual design purpose.

2.4 Statistical RF modeling of in-building distributed-antenna system

2.4.1 Statistical versus "exact" approaches

A principle goal for site-specific radio simulations is to determine proper placement of antennae throughout the building so that adequate radio coverage is guaranteed over virtually all locations within the building. Intuitively, such guarantee can be given **without** performing any detailed simulations **if** a large number of antennae can be employed to "saturate" the building, radio-wise. Performing radio simulation of such a scenario using, for example, WiSE tool [10], will yield a radio power distribution throughout the building with a probability density function (PDF) which approaches a δ -function, as the number of antennae per unit area increases indefinitely. This is not observed in practice since fast-fading due to multipath, and field interference between neighboring antennae, are not taken into account in the simulation. In fact, we will shown below that the radio power PDF will asymptotically approaches a distribution form with finite width. The form of the distribution is largely independent of the detailed floor plan but rather, depends only on a few statistical building parameters which can be easily determined from a given floor plan.

Thus, using the "saturated" design paradigm for in-building distributed-antenna system, the design focus should move from detailed site-specific radio simulation towards understanding and applying these limiting PDF's in the radio statistics. The rest of this section is devoted to this latter subject.

We limit our considerations to the case where all mobile users and antennae elements in the building receive and transmit in the same radio band, i.e., the entire building constitutes a single "cell" in the radio sense. It is assumed that RF signals transmitted by mobile users inside the building are received simultaneously by multiple antenna elements, which are transmitted via analog cable or fiber-optic links to a RF summing node where the signals from all antennae elements inside the building are vector-summed. For the downlink, the RF signals are distributed from the central node to all antenna elements and broadcasted simultaneously. As such, the RF power distribution so derived applies to the site of the mobile user for the downlink and well as uplink. If there are intelligent signal combining techniques at summing node such as those discussed in [17], then the analysis should only applied to the downlink, and alternative analysis should be performed for the uplink.

Extensive simulations, as described below, show that:

1. For a distributed-antenna system in the "saturated" limit (the number of antenna per unit area required to approach this limit will be described later), the resulting radio statistical distribution is largely independent of the exact floor plan.
2. Instead, the "saturated" radio distributions can be accurately predicted from these simple averaged building parameters: the mean (d) and variance (σ^2) of the distances between walls, the average radio power reflection (R) and transmission (T) coefficients of the walls.

The wall separation parameters and can be determined quite easily given the building floor plan. The wall transmission and reflection characteristics can be found from well documented sources if the wall material is known, and otherwise can be determined quite easily through simple measurements. We found that this surprisingly oversimplified approach can produce accurate

results for a wide range of building parameters. We will discuss circumstances under which this simplified approach ceases to be accurate.

2.4.2 Equivalent-grid Model

We demonstrate the validity of the above assertions by taking a typical office floor plan (for illustration, that of Cory Hall at U. C. Berkeley) and calculate the radio statistical distribution by (1) performing an exact ray-tracing calculation on a floor covered by a distributed-antenna system with various number of antennae, and (2) perform the same calculation on a fictitious floor plan which consists of a rectangular grid of walls (Fig. 1). The rectangular grid is uniformly spaced with average x - and y - separations conforming to the corresponding mean wall-separations of the actual floor plan.

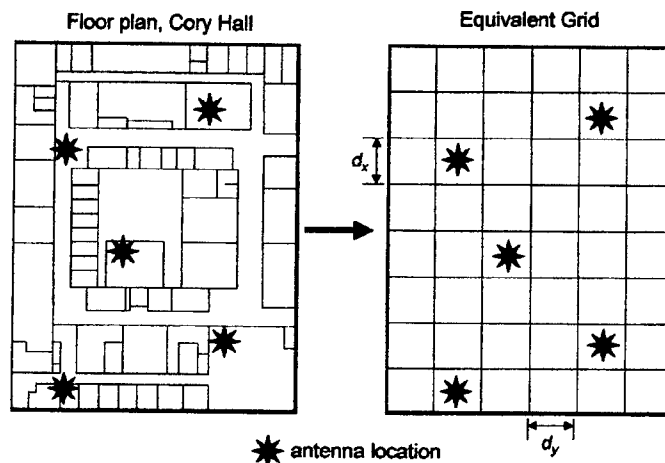


Fig.12 Transformation from original floor plan to equivalent grid.

During the simulation, however, the position of the grid line is displaced from its regular position according to a uniform random variable whose variance also conforms to that of the actual floor plan. The actual building is assumed to be constructed from materials with RF reflection and transmission coefficients of R and T ; the same parameters are used in the fictitious rectangular grid. We note that even though exact ray-tracing are done both on the original floor plan and the fictitious one, the computing time required to complete the simulation for the latter is about an order-of-magnitude less than that of the former, due primarily to the extreme ease of determining the number of walls

traversed by each ray, and locations of image antennae to account for reflection of rays. (We included between 4-8 images (reflections) which we found to be sufficient for convergence of the final result for most building parameters.) The computational resource differential is particularly significant as the number of antenna becomes large.

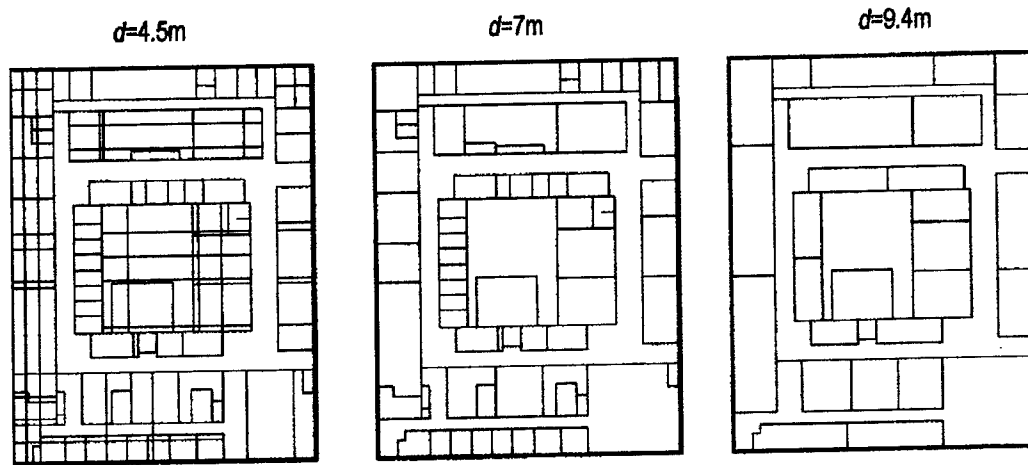


Fig.13 Three floor plans with different average wall separation based on which ray-tracing and grid simulations are done and compared.

The simulation is done at a wavelength of 0.3m, which corresponds to a carrier frequency of 1 0Hz. The resolution of the simulation is one third of the wavelength, which is fine enough to resolve fading effects. The size of the building is 50x65m. We compare three floor plans with mean wall separations of 9.4m, 7m and 4.5m, with standard deviations of 6.8m, 5.9m and 4.5m respectively (see Fig. 2). We also consider (power) reflection coefficients (R) of 0.1, 0.3 and 0.5, with transmission coefficients ($T=1-R$). We explore the effect of deploying 5 to 20 antennae which are placed approximately uniformly across the floor as shown (Fig. 1). It is assumed that the antennae are placed on the ceiling 2m above the observation plane. The simulation is a 2-dimensional propagation simulation based on the vector-sum of fields at the observation point:

$$P = \left| \sum a_i \exp(ikr_i)/r_i \right|^2$$

where P denotes the total power at the observation point, r_i denotes the distance the i th

ray travelling from the antenna/image to the observer (accounting for the 2m vertical separation), a_i denotes the attenuation factor due to the transmission through walls for the i th ray. The total RF power emitted from ALL antennae is assumed to be a constant regardless of the number of antennae, and is uniformly distributed among all antennae.

2.5. Results

The principle results of the simulations are shown in Fig. 3 and 4. Figure 3(a) shows the comparison between the RF power distribution statistics of the actual floor plan and that of the corresponding rectangular grid, for three different floor plans (Fig. 2) with average wall separations of 9.4m, 7m and 4.5m, and for T ranging from 0.9 to 0.5. Five antennae placed according to Fig. 1 are used in this simulation. The fact that it is difficult to differentiate the existence of two curves in most of the plots testify to the surprising accuracy of the grid simulation as compared to that of the real floor plan, for the wide ranges of building parameters used. To further illustrate the degree of match between the two simulations, the same results are plotted as a cumulative distribution function (CDF) in Fig. 3(b) with a logarithm vertical scale. One observes a superb match down to a cumulative statistics of 0.1% at the tail end of the distribution. Four observations are worth noting here:

1. The "smoothness" of the distribution curve is somewhat surprising, for both the simulation involving the actual floor plan and the rectangular grid, but perhaps more so for the former, since the actual floor plan is quite irregular (Fig. 2), and the resulting radio power distribution should also be expected to behave as such. This "smoothness" is largely a consequence of a "large" number of antenna: if the number of antenna is reduced to below 5, irregular spikes can be observed in the radio power distribution. In fact, if a single antenna is used to cover the entire floor, not only is the width of the distribution widened considerable, the distribution itself is very irregular as expected of a complicated internal building structure

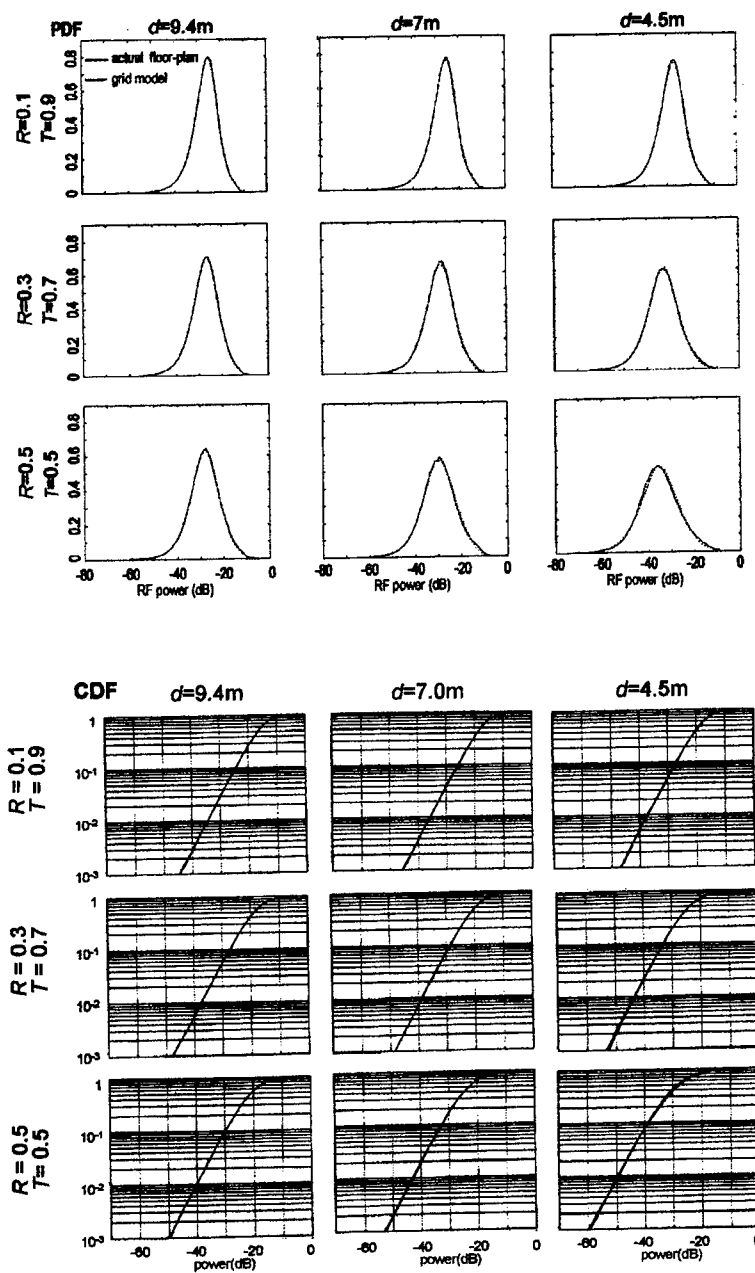


Fig.14 (a) (top) Radio statistics (PDF) comparison for different d , R , T - actual floor plan vs equivalent grid model. (b) (bottom) Radio statistics (CDF) comparison for different d , R , T - actual floor plan vs equivalent grid model.

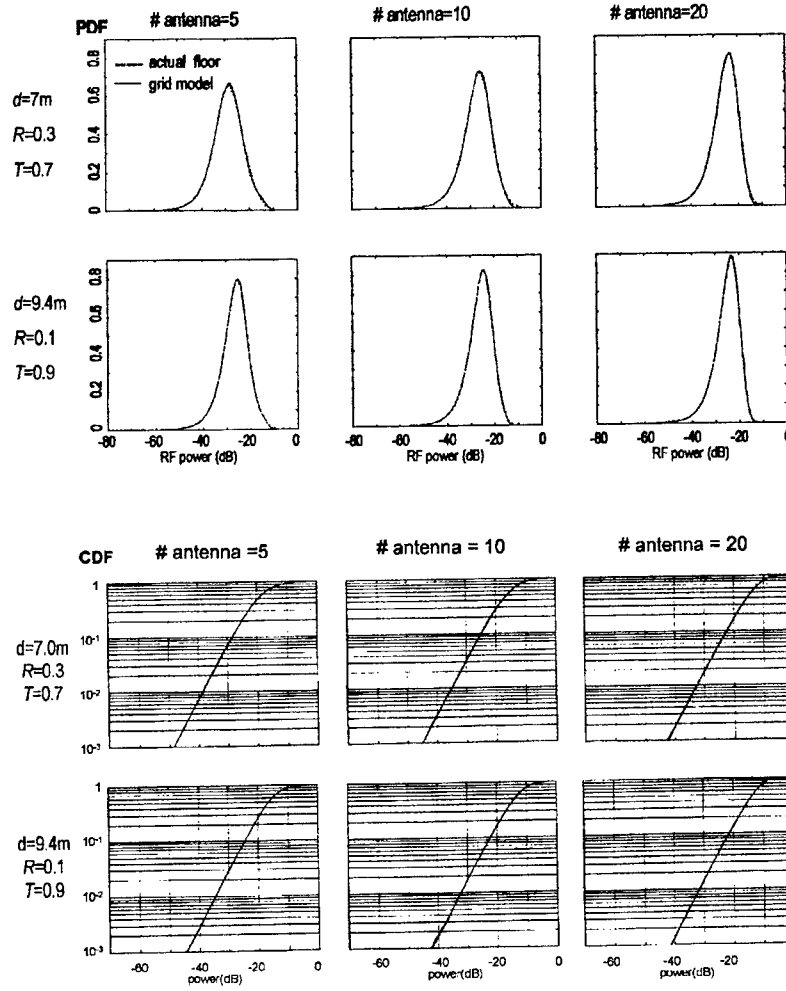


Fig.15(a) Radio statistics (PDF) comparison for two floor plans with different antenna numbers -actual floor plan vs equivalent grid model. **(b)** Radio statistics (CDF) comparison for two floor plans with different antenna numbers -actual floor plan vs equivalent grid model.

2. For system design purpose, it is important to determine the dynamic range D of the received RF power with a given probability q , i.e., for a user randomly located inside the building, the probability being q for the maximum/minimum ratio in the received RF power to be less than D (measured typically in decibel difference). If the hardware comprising the transmit, receive and transport infrastructure of wireless system are designed to have a dynamic range performance of D , then the probability of failure is $b=1-q$, which can be interpreted loosely as *call-blockage probability* or *grade-of-service* of the in-building system. Observing the distribution plots of Fig. 2, one can discern a clear trend towards a narrower distribution (i.e.,

a smaller dynamic range) for a building with larger rooms and lower reflections from walls. This can be intuitively understood since both of these trends tend to diminish effects of radio non-uniformity arising from the internal structure of the building.

3. Thus intuitively, one can expect an empty building with no internal structure at all to have the narrowest RF power distribution, in fact, in the limit of an infinite number of antennae, a δ -function for the PDF. This is not the case in our simulation, as illustrated by the simulation results of Fig. 3 which shows the PDF and CDF of the radio power distributions with the number of antenna/floor increasing from 5 to 20, for two different sets of building parameters. Again, the match between the simulation of the actual floor plan and that of the equivalent grid is impeccable, but the more interesting observation is the limiting distribution to which the PDF(CDF) converges in the limit of a large number of antennae and an empty building (the case of 20 antennae and 9.4m rooms with reflection of 0.1). Further increases in the number of antenna and reduced internal building structure does not lead to significant changes in the distribution. This is due to radio interference between antennae, which produces fading of the RF signal in the space domain. In fact, we show in Section 3 that the distribution in this limit actually approaches a Rayleigh distribution. This is the narrowest distribution one can expect for an in-building environment; any addition of internal structures results in broadening the distribution from the Rayleigh limit.
4. For the grid simulation, the "smoothness" of the radio power distribution is seen only by incorporating the random dithering in the grid positions, as discussed in Section 4 above. The irregularity resulting from simulation of a perfectly rectangular grid *without* random dithering is shown in Fig. 5, and is believed to result from the periodic nature of the reflectors. (As one can see, the effect is more obvious for stronger reflection case.) However, the distribution is not sensitive to the standard deviation of the random dither, as long as it exceeds some value, typically in the 1-2m range. Therefore, in the global characterization of the building, the variance σ^2 of the wall separation is not as important as the other three parameters (mean distance between walls d , reflection and transmission coefficients R and T .)

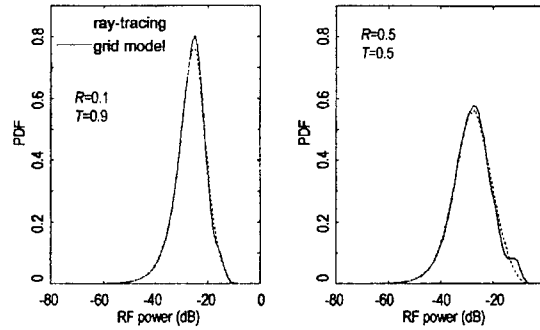


Fig. 16 PDF obtained from ray-tracing of actual floor-plan, and grid model **without** random dithering (simulation done on the 2nd floor of Cory Hall, Fig. 1.) Left: $R=10\%$, $T=90\%$; right: $R=50\%$, $T=50\%$

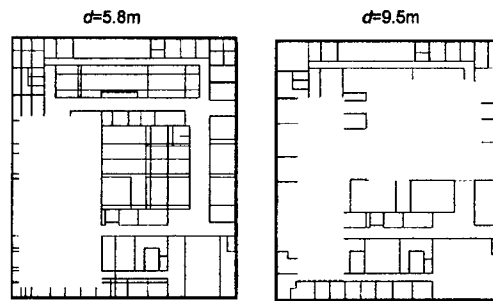


Fig. 17 Two very non-uniform floor plan with average wall separations of 5.8m and 9.5m

5. We have explored whether or not the grid model applies to an actual floor-plan which is highly non-uniform, i.e., there is a big disparity in room sizes in different parts of the building such as those with open atriums and conference halls, as shown in the two floor-plans in Fig. 6. Results of ray-tracing simulations of these actual floor-plans is compared to the equivalent grid model is shown in Fig. 7 (using 5 antennae placed in the same position as that before, see Fig. 1) We observe that, again, the matching is very good for wall reflection coefficients as high as 0.5.

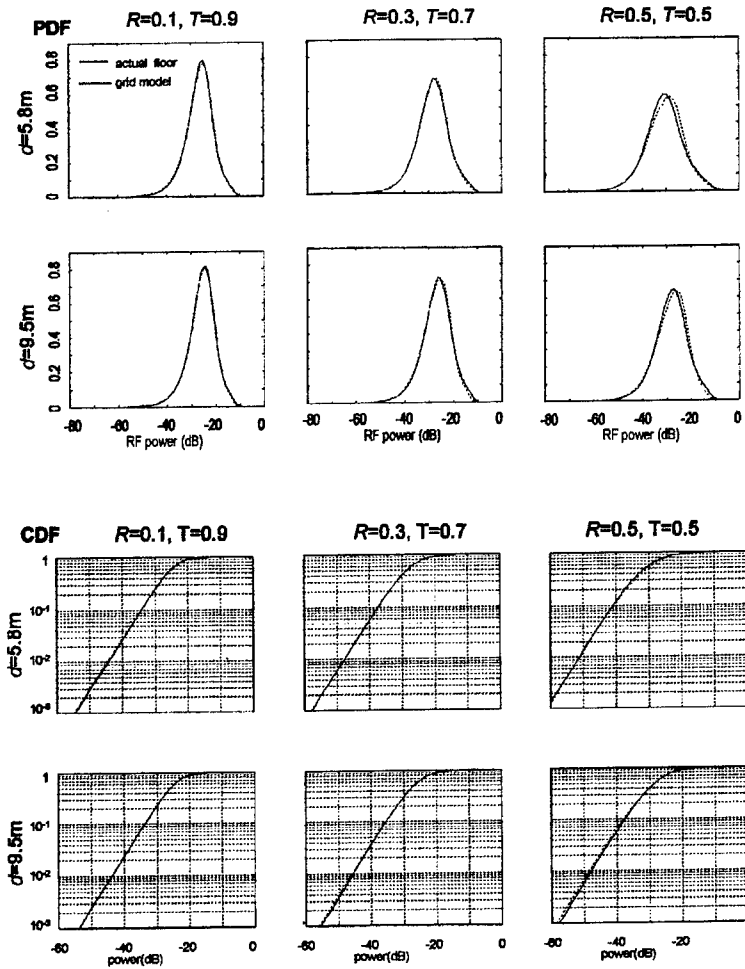


Fig. 18 (a) Radio statistics (PDF) comparison for two very non-uniform floor plans as shown in Fig. 6 with various wall reflections and transmissions - actual floor plan simulation vs equivalent grid model. (b) Corresponding CDF's of those shown in (a)

2.6. Further discussions

From a system viewpoint, the significant aspect of the radio power statistical distribution lies in the low-power tail end of the distribution, since these deep fades corresponds to locations in the building where the received radio power falls outside the dynamic range which the hardware can handle. It impacts directly the grade-of-service of the wireless network. To achieve a 1% grade-of-service (i.e., probability of blocked/dropped calls is below 1%) which is ordinarily considered quite satisfactory for wireless communication, the probability of occurrence of such deep fades should be kept well below 1%. We have shown that increasing the number of antenna can, up to a certain point, reduce the width of the distribution and thus reduces the probability of deep fades. These results are presented again in Fig. 8 in a slightly differently format, in which the probability of the radio power falling below a given factor from the maximum of the distribution, is

plotted against the number of antennae deployed (for a 50x65m building).

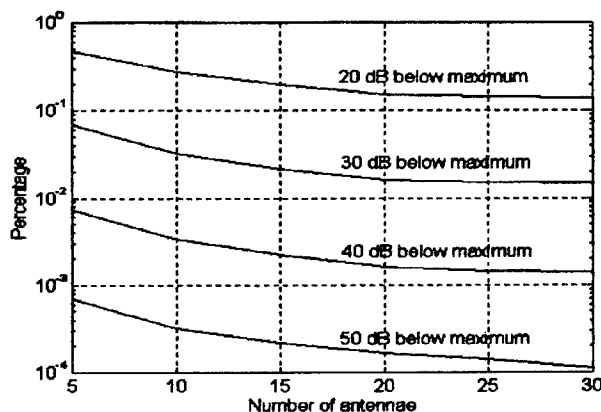


Fig.19 Percentage of tail area of PDF as a function of number of antennae for different thresholds. (for 2nd floor of Cory Hall, $d=7m$, $R=30\%$, $T=70\%$)

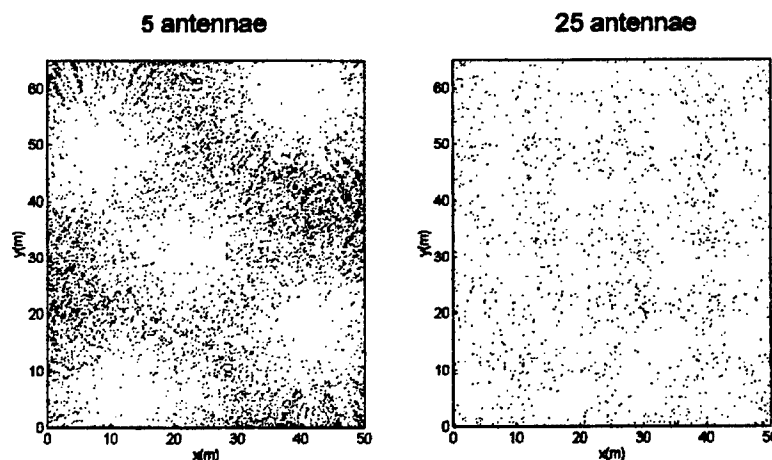


Fig.20 Radio map of locations where power is 35dB below maximum ("deep-fade") for the second floor of Cory Hall. ($d=7m$, $R=30\%$, $T=70\%$) Left: 5 antennae case, percentage of area under "deep-fade", 2%, right: 25 antennae case, percentage 0.4%.

From a mobile user's viewpoint, the spatial distribution of deep fades, in addition to the probability of occurrence, also plays a role in determining the quality of service. Extended zones of poor radio perception tends to be more annoying than occasional bursts of noisy pickup when the user passes through a deep fade of limited spatial extent. To illustrate this aspect of radio reception, the spatial distribution of deep fades, defined here as locations where the received field strength drops below 35dB from the global maximum, is plotted in Fig. 9 for a 5-antenna and a 25-antenna system. For the 5-antenna system, deep fades occur over approximately 2% of floor space, which is reduced to 0.4% for a 20-antenna system. From these plots one can notice that the deep

fades are more scattered for the 25-antenna system.

To further characterize the spatial distribution of deep fades, we plot in Fig. 10 the 2-dimensional spatial autocorrelation of the deep fades with a resolution of 1cm. These plots show that employing a larger number of antennae (approximately 15-25 antenna over a 50x65m floor space) reduces the spatial extent of most deep fades to <4cm. These results illustrate the fact that, since deep fades are caused by near-complete cancellation of field vectors at the observation point due to various antenna sources and multipaths, the spatial extent over which it occurs is reduced as the number of field vectors contributing to the sum increases.

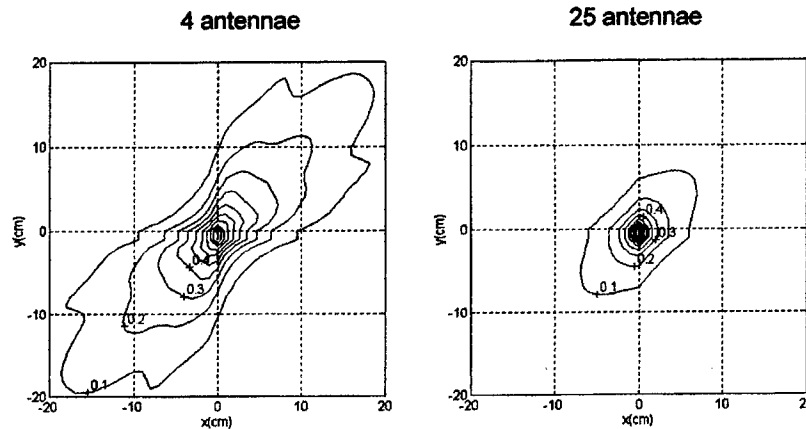


Fig. 21 2-D spatial autocorrelation of deep-fade pattern (defined as locations where RF power is 30 dB below maximum) for a 30m by 30m

2.7. Conclusion

In order to provide uniform radio coverage in indoor environment, implementation of distributed-antenna networks has been proposed. We presented a grid model to calculate the radio power statistics inside a building which is shown to match that of the exact distribute to a very high degree of accuracy. In this model, four parameters - reflection coefficient and transmission coefficient of walls, and average wall distance and its variance, provide a statistical description for the whole building. The first two parameters can be determined from the building types, and the last two parameters can be determined from the floor plan. **There is no adjustable parameter in our model.** The resultant grid model can be simulated very efficiently to give a statistical distribution for the building. The advantage of using a distributed-antenna network to reduce the width of the PDF of the distribution and thus improving system performance can be observed readily, especially in a highly attenuated environment. A further advantage of employing a

distributed-antenna system is the reduction of the physical width of the deep fades to below that of a typical antenna size of a mobile handset, which implies a virtual elimination the effects of deep fades as far as user performance is concerned. The tool we have developed promises to greatly simplify the design of indoor wireless system on the radio coverage inside complex building environment.

2.8 Section Reference:

- [1] W.I.Way, "Optical fiber-based microcellular systems: an overview" IEICE Trans. on Commun., vol. E76B, No.9, pp.1091-1102, 1993
- [2] T.S.Chu, M.J.Gans, "Fiber optic microcellular radio", IEEE Trans. on Veh. Tech., vol.40, No.3, pp.599-606, 1991
- [3] L.J.Greenstein, N.Amitay, T.S.Chu, L.J.Cimini, G.J.Foschini, M.J.Gans, Chih-Lin I, A.J. Rustako, R.A.Valenzuela, G.Vannucci, "Microcells in personal communications systems", IEEE Communications Magazine, Dec 1992, pp.76-88
- [4] A.A.M.Saleh, A.J.Rustako, Jr. and R.S.Roman, "Distributed antennas for indoor radio communications", IEEE Trans. Commun., Vol. COM-35, No.12, pp.1245-51, Dec. 1987
- [5] A.Arredondo, et al, "Techniques for improving in-building radio coverage using fiber-fed distributed antenna networks", IEEE Vehicular Technology Conference, Atlanta, may 1996
- [6] For example, LGCell™, LGC Wireless Inc., San Jose, California.
- [7] D.Molkdar, "Review on radio propagation into and within buildings", IEE Proceedings-H, vol.138, No.1, Feb 1991, pp.61-73
- [8] H.Hashemi, "Indoor radio propagation radio channel", Proceedings of the IEEE, vol.81, No.7, July 1993, pp.941-968
- [9] R.A.Valenzuela, "A ray tracing approach to predicting indoor wireless transmission", Proc. 1993 IEEE 43rd Veh. Tech. Conf., IEEE Press, Piscataway, N.J., 1993, pp.214-218
- [10] S.J.Fortune, D.M.Gay, B.W.Kernighan, O.Landron, R.A.Valenzuela, M.H.Wright, "WiSE design of indoor wireless systems: practical computation and optimization", IEEE computational Science and Engineering, pp.58-68, Spring 1995
- [11] K.R.Schaubach, N.J.Davis, T.S.Rappaport, "A ray-tracing method for predicting path loss and delay spread in microcell environments", Proceedings of the 1992 IEEE Veh. Tech. Society Conf., Denver, pp.932-935, May 1992
- [12] R.H.Clark, "A statistical theory of mobile-radio reception," Bell Syst. Techn. J., vol. 47, pp. 957-1000, July-Aug., 1968

- [13] S.O.Rice, "Mathematical analysis of random noise", Bell Syst. Tech. J., **vol.23**, pp.282-332, 1944 and **vol.24**, pp.46-156,1954
- [14] M. Nakagami, "The m-distribution---a general formula of intensity distribution of rapid fading," in **Statistical Methods of Radio Wave Propagation**. Pergammon Press, 1960
- [15] "Received signal fading distributions," IEEE Trans. Vehicular Techn., **vol.37**, no.1, Feb. 1988
- [16] H. Suzuki, "A statistical model for urban radio propagation," IEEE Trans. Commun. **Vol. COM-25**, pp. 673-680, July 1977
- [17] J.H. Winters, J. Salz and R. D. Gitlin, "The impact of antenna diversity on the capacity of wireless communication systems", IEEE Trans. Commun., **Vol. 42**, pp. 1740-51, 1994.

3. In-building Radio Distribution Using a "Saturated" Distributed-Antenna Architecture - Analytic Approach

Section abstract

Section 2 described properties of in-building radio distribution statistics under a "saturated" distributed-antenna scenario. The *independence* of the asymptotic radio-distribution statistics on specific floor plan lends the opportunity to derive these results analytically, thereby adding insight and understanding to the problem. The key assumption in the analytic approach is that when the number of antenna elements per unit area becomes large, we can approximate the discrete antennas by a uniform and continuous blanket of antenna. The validity of the assumption is established by observing the fact that the analytic results so derived conform extremely well to that from the computer simulation of Part I, even for a surprising small number of antennae per unit area. Again, the excellent match is obtained with **no adjustable parameters** in the model.

3.1. Introduction

Distributed-antennas are deployed in indoor wireless microcell to provide uniform radio coverage. With multiple antennas simultaneously transmitting (or receiving) RF signals, the radio signal received (or sent) by a mobile user anywhere in the microcell is the vector sum of the radio signals transmitted (or received) by each spatially located antenna. The phases of these component antenna signals depends on the relative distance between the mobile user and the antennae, and on the length of the cables interconnecting the antennae and the summing node. As a result, local fading may occur due to the interference between different antenna signals. While the global radio coverage tends to become more uniform with increasing number of antennae, local power variations due to antenna interference will become more significant. We have shown through simulation, in Section 2, that beyond a certain antenna "density", the global radio statistical distribution converges to a distribution which is largely independently of the detailed floor plan of the building but can be predicted with a high degree of accuracy using only a few global building parameters. The purpose of Part II is to provide some analytical basis for this property, and to derive through analysis the converging radio distributions obtained by simulations in Part I. It was found that excellent agreement can be obtained between the simulation results and the analytical results, over a large range of building parameters, and again with no adjustable parameters in the

model. These approaches and results could lead to a better basic understanding of the problem of radio propagation in a complex, in-building environment.

To grasp the essence of the problem without unnecessary complications, we make the following key assumptions:

1. We approximate the discrete antennae in a distributed antenna system by a *continuous* blanket of antennas of uniform density. The total number of antennae in the system is the density times the area covered by the whole distributed antenna system, nominally, one floor of a building or parts thereof (the "cell"). This assumption is clearly valid when the total number of antennas inside the cell is very big. To see the limit of validity of the assumption, the result so derived will be checked against actual simulation of the floor plan with discrete antenna elements. As reported below, a surprisingly good match was observed for as little as 5 antennae covering a floor space of $50 \times 50 \text{m}^2$.
2. We assume the cell is infinitely extended and the cell boundary condition is thus of no concern. In practice, when the radio power decays rapidly from its point of origin due to partitions and scatterers as typical in an indoor wireless environment, only those antennae close to a mobile user contributes significantly to the radio reception. If this characteristic distance is small compare to the dimension of the cell, then from each user's point of view the cell is infinitely extended.

Other approximations are more mathematical in nature and will be mentioned as they arise in the analysis.

It should be reminded that the results derived below applies to the scenario where the uplink RF signals received at the antenna elements are simply vector-summed at a central node in the building, and the downlink RF signals are similarly broadcasted from the central node. More intelligent combining techniques require additional consideration for the uplink.

The section is organized into the following sections. In Section 2.2 we introduce some mathematical background and consider the case where there are no partitions inside the building (an empty building). In Section 2.3, we derive a theoretical model for the received signal amplitude distribution in a building partitioned by a rectangular grid of walls (which is used in the simulations of Section 2.2). We then show in Section 2.4 the excellent match between the result

using the theoretical model and that from the computer simulation, again, with no adjustable parameters in the models. We conclude in Section 2.5.

3.2. Empty cell model

3.2.1 Rayleigh's random flights[1]

A basic mathematical result to be used in subsequent analysis concerns the statistical distribution of the sum of n random vectors. Consider a two-dimensional random vector $\vec{x} = (x_1, x_2)$ where both x_1 and x_2 are random variables. The corresponding characteristic function is defined as

$$\bar{E}(e^{i\xi_1 x_1 + i\xi_2 x_2}) = \varphi(\xi_1, \xi_2) \quad (1)$$

where \bar{E} stands for expectation. Now consider the sum of n independent vectors of the same magnitude x . For each one of them, in polar coordinates, i. e. with the definitions

$$x_1 = x \cos \Phi, x_2 = x \sin \Phi, \xi_1 = \xi \cos \theta, \xi_2 = \xi \sin \theta, \quad (2)$$

we rewrite the characteristic function as

$$\varphi(\xi) = E(e^{i\xi x \cos(\theta - \Phi)}) \quad (3)$$

where Φ is the random variable denoting the direction of the vector. Since each random vector is issued in a random direction, Φ should be uniformly distributed over 0 to 2π . The characteristic function of a single random vector is then

$$\varphi(\xi) = \frac{1}{2\pi} \int_0^{2\pi} e^{i\xi x \cos(\theta - \Phi)} d\Phi = J_0(x\xi) \quad (4)$$

where J_0 is the Bessel function of 0th order. Since each random vector is independent, the characteristic function of the sum of n random variables is the product of the individual characteristic functions of the random variables, i. e. $J_0^n(x\xi)$.

To obtain the probability density function (PDF) $f(x_1, x_2)$ of the random vector $\vec{x} = (x_1, x_2)$, one inverse Fourier transform the characteristic function $\varphi(\xi)$:

$$f(x_1, x_2) = \frac{1}{4\pi^2} \int_0^\infty \int_0^\infty d\xi_1 d\xi_2 \varphi(\xi_1, \xi_2) e^{-i(\xi_1 x_1 + \xi_2 x_2)}. \quad (5)$$

Since $\varphi(\xi_1, \xi_2)$ depends only on $\xi = \sqrt{\xi_1^2 + \xi_2^2}$, we can again use the polar coordinates with

$$x_1 = x \cos \theta, x_2 = x \sin \theta, \xi_1 = \xi \cos \phi, \xi_2 = \xi \sin \phi \quad (6)$$

and express the PDF as

$$f(x_1, x_2) = f(x) = \frac{1}{4\pi^2} \int_0^\infty \xi \varphi(\xi) d\xi \int_0^{2\pi} e^{-ix\xi \cos(\phi - \theta)} d\phi = \frac{1}{2\pi} \int_0^\infty \xi \varphi(\xi) J_0(x\xi) d\xi. \quad (7)$$

Noting that the $f(x_1, x_2)$ is a function of the magnitude of the random vector $x = |\vec{x}|$ only, the PDF of $x = |\vec{x}|$ is thus

$$p(x) = 2\pi x f(x) \quad (8)$$

3.2.2 Probability density function of RF amplitude distribution inside cell

Here we consider the case where there are no partitions inside the cell, and each antenna is omnidirectional. Again, we assume a 2-dimensional propagation model where reflections from the floor and ceiling are neglected. The amplitude of the RF signal is assumed to decay as $1/r^\alpha$ where r is the distance between the source antenna and the observation point and α is the decay constant that is used in practice to characterize the power decay in an indoor wireless environment[2-4]. We require $\alpha > 1$. It is further assumed that the cell is big so that the reflection from the cell boundary at any observation point inside the cell is negligible. The received RF signal at any particular point inside the cell is thus the sum of signals from all the antennas in the cell.

The signal at a particular observation point may be expressed as

$$E = \sum_k \frac{A}{r_k^\alpha} e^{i(\omega t + \Phi_k)} = e^{i\omega t} \sum_k \frac{A}{r_k^\alpha} e^{i\Phi_k} \quad (9)$$

where the summation runs over all the antennas in the cell. The constant A is a measure of signal amplitude emitted from each individual antenna (assuming all antennae are identical), ω is the RF carrier frequency. The phase Φ_k changes by 2π when the distance changes over a wavelength of the carrier, which is much smaller than the dimension of the cell. Hence for different observation points, Φ_k can be considered as a random variable uniformly distributed over 2π . The received signal amplitude at the observation point is then

$$|E| = \left| \sum_k \frac{A}{r_k^\alpha} e^{i\Phi_k} \right| \quad (10)$$

To find the PDF of $|E|$ we first find the characteristic function of the random vector E and obtain the PDF by Fourier transform.

We first consider the contribution from the antennas in the differential annulus at a distance r from the observation point as shown in Fig. 1. The total number of antennas in the band

is calculated as $N = \mu 2\pi r dr$ where N is the number and μ is the antenna density. The resulting summation of the field contribution from these antennae is

$$\sum_{k=1}^N \frac{A}{r^\alpha} e^{i\Phi_k} \quad (11)$$

Since Φ_k is a random variable uniformly distributed over 2π , the summation is similar to the vector sum in the Rayleigh's Random Flights as discussed in Section 1.1. The corresponding characteristic function is $J_0^N((A/r^\alpha)\xi)$. If we assume μ is large so that $N \gg 1$, we can always make N an even number by adjusting dr so that

$$J_0^N((A/r^\alpha)\xi) = |J_0((A/r^\alpha)\xi)|^N = e^{\mu 2\pi r dr \log |J_0((A/r^\alpha)\xi)|} \quad (12)$$

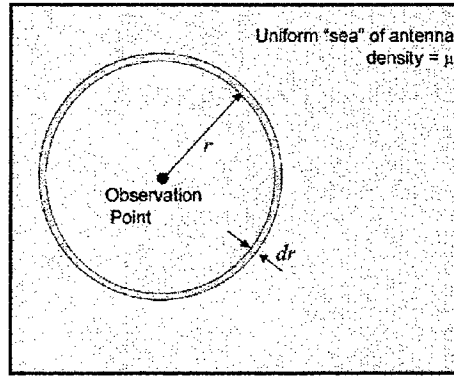


Fig.22 Empty-cell model.

Since the total field contribution from all the antennae in the cell is the sum of contribution from all annuli, the characteristic function of the total field is thus the product of the individual characteristic functions:

$$\varphi(\xi_1, \xi_2) = \varphi(\xi) = e^{2\pi\mu \int_0^\infty r dr \log |J_0(A\xi/r^\alpha)|} = e^{(2\pi\mu A^\alpha \xi^\alpha / \alpha) \int_0^\infty y^{-(1+2/\alpha)} \log |J_0(y)| dy} \quad (13)$$

where in the last equality we replaced the r by $y = A\xi/r^\alpha$.

It is shown in the Appendix that the integration

$$\int_0^\infty y^{-(1+2/\alpha)} \log |J_0(y)| dy$$

(14)

converges to a negative constant $-C_0$ where $C_0 > 0$. The characteristic function is thus rewritten as:

$$\varphi(\xi) = e^{-(2\pi\mu C_0 A^{\frac{2}{\alpha}} / \alpha) \xi^{\frac{2}{\alpha}}} \quad (15)$$

The PDF of received signal \vec{E} is obtained by inverse Fourier transformation of the characteristic function as described in Section 1.1. Using Eq. (?), the PDF for the total received field amplitude $E=|\vec{E}|$ is thus

$$p(E) = x \int_0^\infty \xi J_0(E\xi) e^{-(2\pi C_0 A^{\frac{2}{\alpha}} / \alpha) \xi^{\frac{2}{\alpha}}} d\xi \quad (16)$$

3.2.3 PDF for two special cases

For power decay characteristic $\alpha=1$ (corresponding to the case when there is no propagation loss within the cell), the characteristic function is a Gaussian $e^{-(2\pi\mu C_0 A^2) \xi^2}$, and the PDF of the received RF amplitude PDF becomes

$$p(E) = \frac{E}{b} e^{-\frac{E^2}{2b}} \quad (17)$$

which is the Rayleigh distribution with the characteristic parameter $b = 4\pi\mu C_0 A^2$. If $\alpha = 2$ (power decays as r^{-4}), the characteristic function becomes $e^{-(\pi\mu C_0 A) \xi}$ and the resulting PDF is

$$p(E) = \frac{cE}{(E^2 + c^2)^{3/2}} \quad (18)$$

with characteristic parameter $c = \pi\mu C_0 A$. For other decay characteristic α , closed form of $p(x)$ is difficult to obtain. These two limiting cases for the PDF's are illustrated in Fig. 2. In general, the Rayleigh distribution has a small variance. This follows from the fact that an inverse-square law in power propagation is indicative of absence of absorbers or scatterers in the cell and thus the overall power distribution tends to be more uniform. In fact, in our 2-D distributed-antenna approximation, one can expect the Rayleigh distribution as the limiting case with the smallest possible variance.

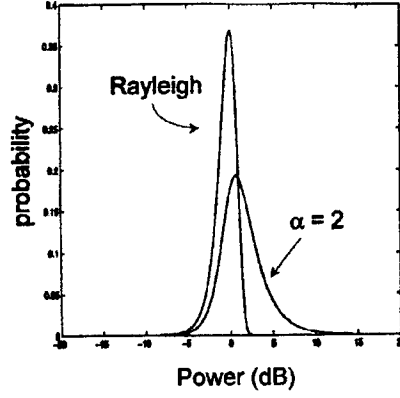


Fig. 23 Two limiting cases of the RF statistical distribution in the "empty-cell" model.

3.2.4 Central limit interpretation

The central limit theorem also applies here. We consider the case when the antenna density μ approaches infinity. A slight modification is however needed, since when the antenna density approach infinity, there exist in an infinitesimally small area around an observation point an infinite number of antennas, which results in infinite received power. To resolve this mathematical difficulty, we apply a practical consideration to our model. Since there exists a finite spacing between users on the floor and antennae located on the ceiling, we introduce a vertical distance h between user observation points and antennae, resulting in the actual distance being $\sqrt{r^2 + h^2}$ where r is the horizontal distance between the user and the antenna. We shall also require the total RF radiated power from all antennae in the cell to be finite and constant. Thus the normalized RF amplitude emitted from each antenna is $A = 1/\sqrt{\mu}$.

With the above modifications, the characteristic function becomes

$$\varphi(\xi) = e^{2\pi\mu \int_0^\infty r dr \log |J_0(A\xi/\sqrt{\mu(r^2+h^2)})|} = e^{(2\pi\mu\xi^2/\alpha) \int_0^{\xi/h^\alpha} y^{-(1+2/\alpha)} \log |J_0(y/\sqrt{\mu})| dy} \quad (19)$$

where, in the last equality, $y = \xi / (r^2 + h^2)^{\alpha/2}$. When μ approaches infinity, we can approximate

$$\log |J_0(y/\sqrt{\mu})| \approx \log(1 - \frac{y^2}{4\mu}) \approx -\frac{y^2}{4\mu} \quad (20)$$

resulting in the characteristic function:

$$\varphi(\xi) = e^{\lim_{\mu \rightarrow \infty} (2\pi\mu\xi^2/\alpha) \int_0^{\xi/h^\alpha} y^{-(1+2/\alpha)} (-\frac{y^2}{4\mu}) dy} = e^{-\frac{\pi\xi^2}{4(\alpha-1)h^{2\alpha-2}}} \quad (21)$$

which is a Gaussian as expected from the central limit theorem. The resulting PDF of received signal amplitude, regardless of the decay characteristic α , is Rayleigh with parameter

$$b = \frac{\pi}{4(\alpha - 1)h^{2\alpha-2}}.$$

3.3. Cell with Grid Walls

Actual building floor-plans are complex and irregular so that they do not lend themselves to analytical derivation of radio propagation characteristics. However, the results of Part I show that in the saturated distributed antenna scenario, the global radio statistics do not depend on the exact floor plan, in fact, a overly simplistic floor-plan consisting of a rectangular grid yields results which are amazingly close to that of the actual floor-plan. This empirical property brings forth the possibility of analytical derivation of the asymptotic statistical distributions computed in Part I by analyzing the rectangular grid instead of the complex actual floor-plan.

The grid model is shown in Fig. 3. For illustrative purpose, the vertical and horizontal walls in the figure are equally spaced with distances x_0 and y_0 respectively. In the analysis, however, we don't require the walls to be exactly equally spaced and x_0 and y_0 represent the average distances between walls.

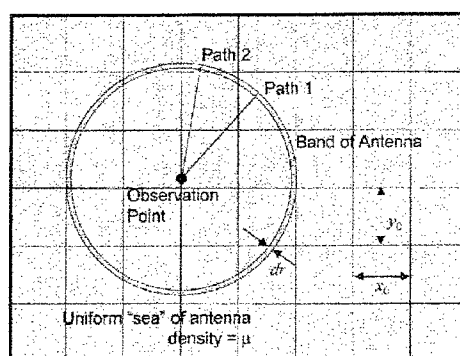


Fig. 24 Model with grid walls. Paths 1 and 2 show that the path loss is direction-dependent.

In the presence of the walls in the cell, the signal propagation loss from the source antenna to the observation point will depend on the number of walls encountered in the propagation path. Moreover, the signal at each observation point is composed of not only the signals from the source antennas but also the reflections from different walls which, equivalently, can be represented by

images antennae generated by the original antennas upon reflections from different walls. A further complication is that for each observation point, only a subset of all image antennae is effective.

We shall perform the analysis in three steps. First, we ignore the image antennae by assuming the reflection is very small. The effect of image antennae is then included, using a simplistic assumption that the image antennae are uniformly distributed throughout the cell. This is not rigorously correct, but, curiously, gives a better fit to the actual simulation results than the exact approach, which is to take the rigorous spatial distribution of the image antennae into account.

3.3.1 Analysis with No Images

In the presence of grid walls, the path loss is directional as shown in Fig. 3. For Path 1 as drawn, there are 5 walls encountered. If each wall has an amplitude transmission factor $t = \sqrt{T}$, then the resulting field amplitude at the observation point is At^4/r . In general, if the observation point is at $(0,0)$ and the source antennae are at (r, θ) in polar coordinates, the resulting field at the observation point due to the source antennae is

$$E = e^{\log t \left(\frac{r \cos \theta}{x_0} + \frac{r \sin \theta}{y_0} \right)} \quad (22)$$

It is assumed here that the transmission and reflection coefficients of the walls do not depend on the incident angle. Since the characteristic function of the sum of the signals from the antennas in the differential area $rd\theta dr$ is $e^{\mu rd\theta \log J_0(E\xi)}$, the received field amplitude characteristic function can be calculated as

$$\varphi(\xi) = e^{\mu \int_0^\infty r dr \int_0^{2\pi} d\theta \log J_0(E\xi)} = e^{4\mu \int_0^\infty r dr \int_0^{\pi/2} d\theta \log \left| J_0 \left(\frac{e^{\kappa r \cos(\theta - \theta_0)}}{\sqrt{r^2 + h^2}} \xi \right) \right|} \quad (23)$$

where constant $\kappa = \log t \cdot \sqrt{1/x_0^2 + 1/y_0^2}$ can be interpreted as the average differential transmission per unit distance and $\theta_0 = \tan^{-1}(x_0/y_0)$ and where we still assume the antennae are at a distance h above the ground. The PDF of received field amplitude is then

$$p(E) = E \int_0^\infty \xi d\xi J_0(E\xi) e^{4\mu \int_0^\infty r dr \int_0^{\pi/2} d\theta \log \left| J_0 \left(\frac{e^{\kappa r \cos(\theta - \theta_0)}}{\sqrt{r^2 + h^2}} \xi \right) \right|} \quad (24)$$

3.3.2 Analysis with a uniform distribution of image antennae

In this scenario, the resulting field amplitude at observation point (0,0) due to image antennas at (r, θ) is

$$E = \frac{\sqrt{1-t^2}}{t} e^{\log t \left(\frac{r|\cos \theta|}{x_0} + \frac{r|\sin \theta|}{y_0} \right)} \quad (25)$$

where the additional factor (compare to Equation (21)) is due to the fact that the image antennae emits an equivalent field strength equal to the reflection coefficient of the wall. If we assume that the walls are dithered from their regular grid positions randomly (as explained in Part I) so that the image antennas are phase-independent of the original antennas, the characteristic function is then the product of that of the original antennas and that of the image antennas, i.e.

$$\varphi(\xi) = [\varphi(\xi)]_{\text{original}} \cdot [\varphi(\xi)]_{\text{image}} = e^{4\mu \int_0^\infty r dr \int_0^{\pi/2} \log \left[\left| J_0 \left(\frac{e^{i\pi} \cos(\theta-\theta_0)}{\sqrt{r^2+h^2}} \xi \right) \right| \cdot \left| J_0 \left(\frac{\sqrt{1-t^2}}{t} \frac{e^{i\pi} \cos(\theta-\theta_0)}{\sqrt{r^2+h^2}} \xi \right) \right| \right] d\theta} \quad (26)$$

The PDF of the received signal amplitude is then

$$p(E) = E \int_0^\infty \xi J_0(E\xi) e^{4\mu \int_0^\infty r dr \int_0^{\pi/2} \log \left[\left| J_0 \left(\frac{e^{i\pi} \cos(\theta-\theta_0)}{\sqrt{r^2+h^2}} \xi \right) \right| \cdot \left| J_0 \left(\frac{\sqrt{1-t^2}}{t} \frac{e^{i\pi} \cos(\theta-\theta_0)}{\sqrt{r^2+h^2}} \xi \right) \right| \right] d\theta} d\xi \quad (27)$$

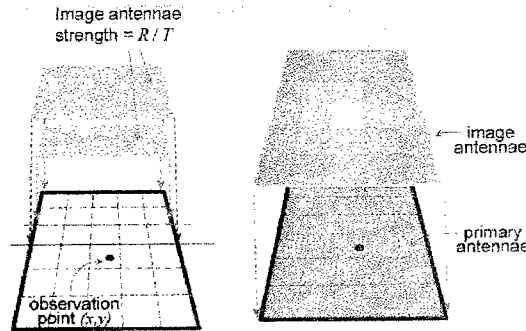


Fig.25 Illustration of image antenna distribution where the original antenna is uniformly distributed, and only one reflection from the grid walls is taken into account.

3.3.3 Rigorous treatment of image antennae

A more rigorous approach can be taken if we limit the analysis to include only the image antennae resulting from a single wall reflection. Let the observation point be (0,0) and Consider the image antenna of the an actual antenna placed at (x,y) as shown in Fig 4. The effective image

antenna density due to horizontal walls is the overlay of half-planes of image antennae due to successive walls, and thus the density of image antennae increases approximately as

$$\frac{y}{y_0} \mu \quad (28)$$

where y_0 is distance between horizontal walls and μ is the real antenna density. In general the effective first-order (single reflection) image density at (x, y) is

$$\mu \left(\frac{x}{x_0} + \frac{y}{y_0} \right). \quad (29)$$

and the effective first-order image antenna density in the differential area $rd\theta dr$ is then

$$\mu r dr d\theta \left(\frac{r|\cos \theta|}{x_0} + \frac{r|\sin \theta|}{y_0} \right). \quad (30)$$

The characteristic function (25) thus becomes

$$\varphi(\xi) = e^{4\mu \int_0^\infty r dr \int_0^{\pi/2} \log \left| J_0 \left(\frac{e^{ir \cos(\theta-\theta_0)}}{\sqrt{r^2+h^2}} \xi \right) \right| d\theta} \cdot e^{\frac{4\mu}{r_0} \int_0^\infty r^2 dr \int_0^{\pi/2} \cos(\theta-\theta_0) \log \left| J_0 \left(\frac{\sqrt{1-t^2} e^{ir \cos(\theta-\theta_0)}}{t \sqrt{r^2+h^2}} \xi \right) \right| d\theta} \quad (31)$$

where $r_0 = \sqrt{x_0^2 + y_0^2}$. The PDF of received signal amplitude is then

$$p(E) = E \int_0^\infty \xi J_0(E\xi) e^{4\mu \left(\int_0^\infty r dr \int_0^{\pi/2} \log \left| J_0 \left(\frac{e^{ir \cos(\theta-\theta_0)}}{\sqrt{r^2+h^2}} \xi \right) \right| d\theta + \frac{1}{r_0} \int_0^\infty r^2 dr \int_0^{\pi/2} \cos(\theta-\theta_0) \log \left| J_0 \left(\frac{\sqrt{1-t^2} e^{ir \cos(\theta-\theta_0)}}{t \sqrt{r^2+h^2}} \xi \right) \right| d\theta \right)} d\xi. \quad (32)$$

3.4. Comparison with Simulation

The results obtained in Section 3 are checked against computer simulations of the rectangular grid model. Since, in Part I, we have established the statistical agreement between the grid model and the actual floor-plan, agreement of the analytic results derived above implies an agreement with the results from the simulation of the actual floor-plan. First, the PDF expression (24) derived from the image-less model is examined for high transmission (90%) as shown in Fig. 5(a) where the average wall distance in both horizontal and vertical direction is 7 meters. An excellent match is clearly observed. The discrepancy between the theoretical expression (24) and real simulation becomes significant when the wall transmission is low (or when the reflection is high) as shown in Fig. 5(b) and 5(c) where the transmissions are 70% and 50% respectively. The

reason for this discrepancy is clearly due to the neglect of image antennae which cannot be ignored at high reflections.

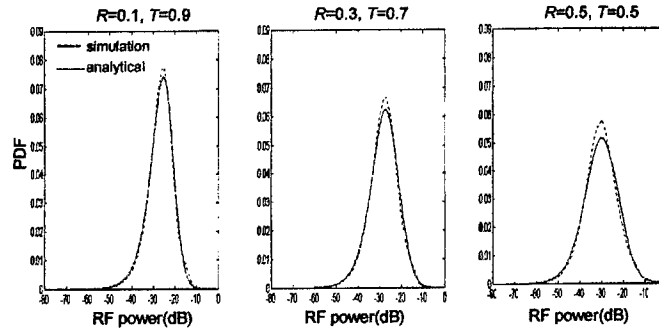


Fig. 26 Radio statistics comparison for different R (wall reflection coefficient) and T (wall transmission coefficient) where the dotted curve shows the ray-tracing simulation result as shown before in Part I, and the solid curve is result using Equation (24) without image consideration. The average wall distance is 7 meters and total number of antennas is 5.

On the other hand, the PDF of Eq. (26) which takes into account of a single overlaying layer of uniformly distributed image antennas shows excellent match with simulation for almost all the wall transmissions from as low as 50% up to 90%, and for different average wall distances as shown in Fig. 6. To illustrate the degree to which the agreement holds, the commutative density function (CDF) of the corresponding PDF's in Fig. 6 are plotted in Fig. 7 down to a probability of 10^{-3} . It is interesting to note that, this excellent agreement is obtained for as little as 5 antenna covering an area of $50 \times 50 \text{m}^2$. As expected, the agreement only improves with a higher density of antenna, as illustrated in the PDF, and the corresponding CDF plots in Figures 8 and 9 respectively.

It is a curious fact that the "rigorous" results of Eq. (32), which properly accounts for reflections of the antennae from successive walls, do NOT agree as well as that of a uniform layer of image antennae as represented by Eq. (26). The reason of this discrepancy is not well understood at this point. However, taking these results at face value, the analytical model of a uniform layer of image antennae yields such excellent matching to the simulation of the rectangular grid floor-plan (and thus the actual floor-plan, per results of Part I) that it can be utilized to predict radio statistics of a building covered with a "saturated" distributed antenna network, to a high degree of certainty.

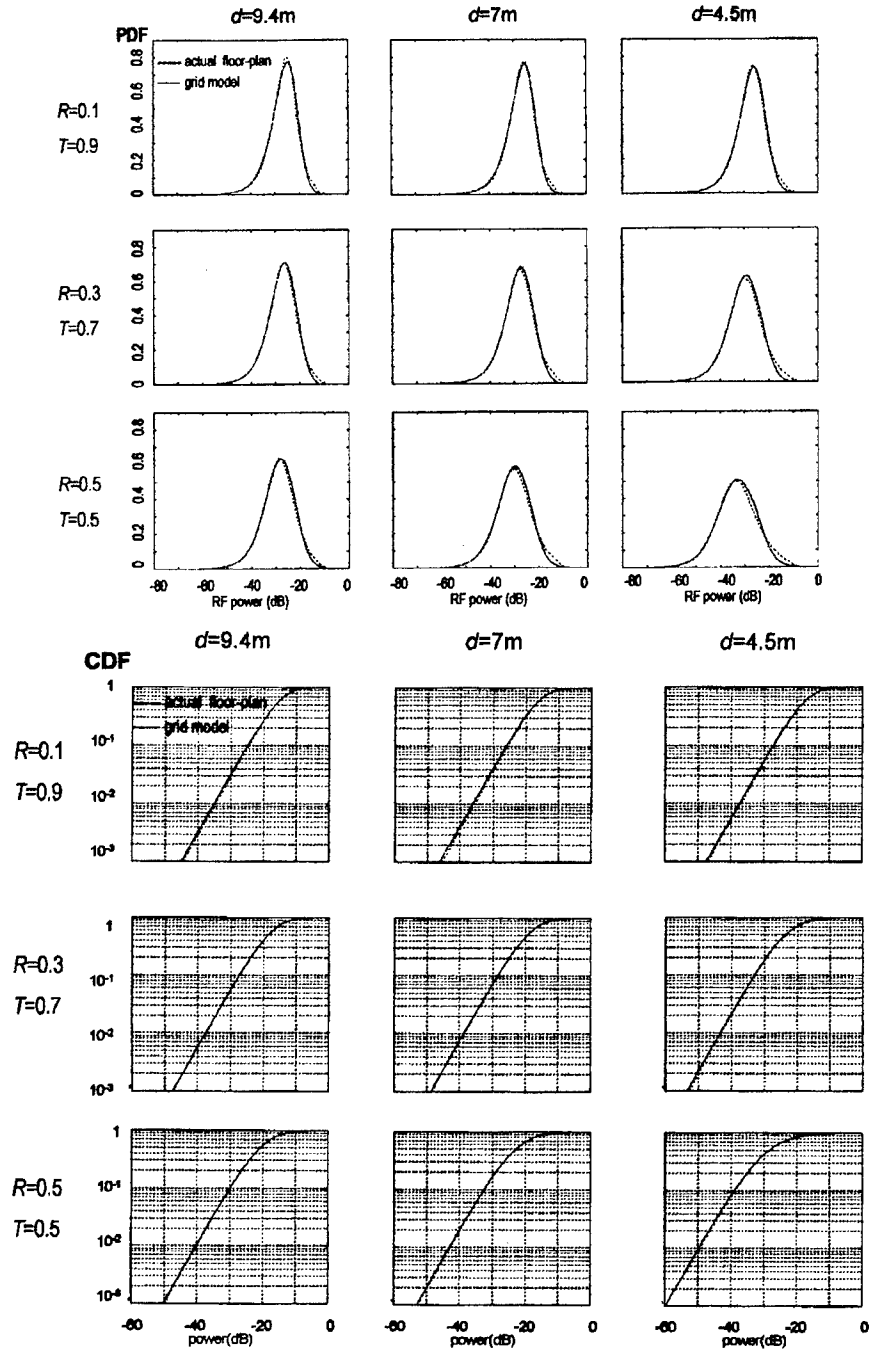


Fig. 27 (a) Radio statistics (PDF) comparison for different d (average wall distance), R (wall reflection coefficient), and T (wall transmission coefficient) where the dotted curve is the result from ray-tracing simulation as shown before in Part I, and the solid curve is the result using Equation (26). The total number of antennas is 5. (b) CDF's corresponding to the PDF's in (a).

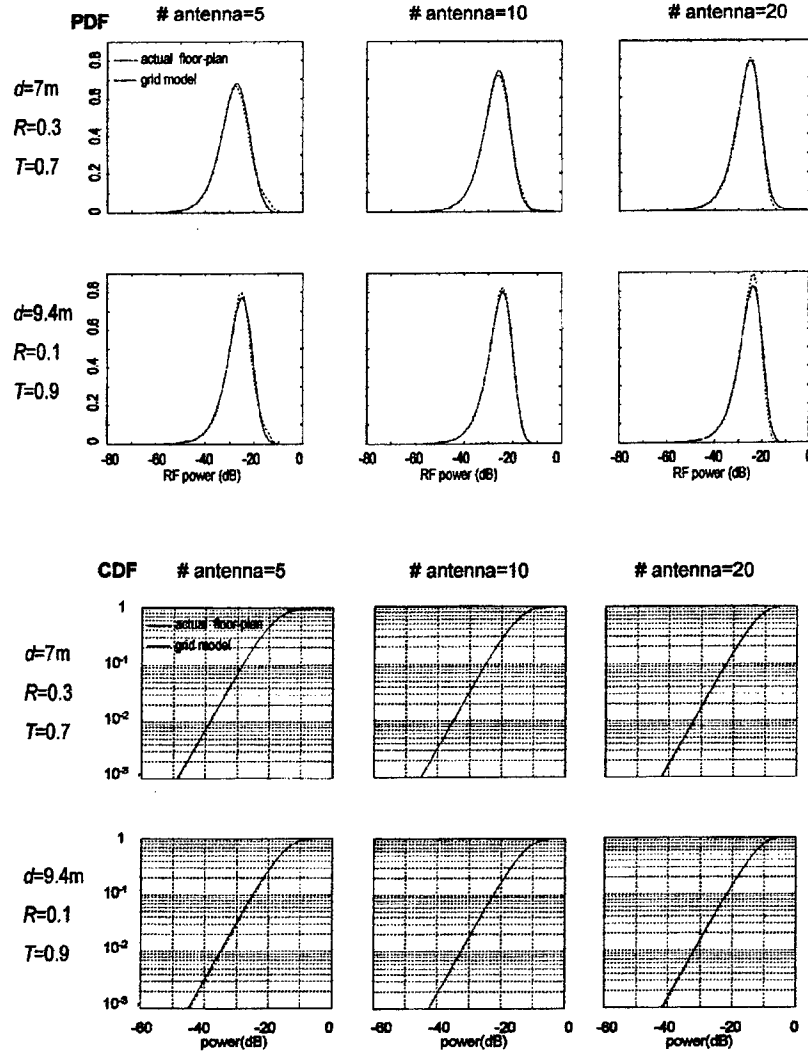


Fig.28(a) Radio statistics (PDF) comparison for different antenna numbers where d , R , T is similarly defined as in Fig. 6 and where dotted curve is simulation result and solid curve is the theoretical result using Equation (26). (b) Corresponding CDF's.

3.5. Conclusion

A theoretical model for received RF statistical distribution in indoor wireless environment with a "saturated" distributed-antenna network is presented in this section. Starting from the Rayleigh's theory, we first derived the signal distribution in an empty cell under the assumption that the antennas are "continuously" and uniformly distributed in the cell (a truly distributed antenna). We deduced closed-form expressions for the distribution for different decay characteristics inside the cell. The distribution derived conforms to the central limit theorem when the antenna density approaches infinity. We then extended the analysis to consider the case where

there are rectangularly-grided walls inside the cell. We derived models with and without considering antenna images. The model derived by assuming a uniform image antenna density conforms very well to the computer simulation. The approach taken and models derived in the section can be used to explain some observed fact in Section 2 and help deepen the understanding on the complex indoor radio coverage problem.

3.6 Appendix : Proof of the Convergence of $\int_0^\infty y^{-(1+2/\alpha)} \log|J_0(y)| dy$

We prove the above integral converges to a negative constant. Since $J_0(y)$ is never bigger than 1, it is obvious that the above expression evaluates to a negative value. In the following, we first prove the integration converges at $y = 0$. We then show the integration is also finite at each singularity of $\log|J_0(y)|$. Finally we prove the convergence of the integration at infinity.

Consider the behavior of the integrand around 0. When y is very small, we notice that

$$\log|J_0(y)| \sim -y^2 \quad (\text{A1})$$

and so the integrand behaves like

$$-y^{1-2/\alpha} \quad (\text{A2})$$

If we assume $\alpha > 1$ (inverse square law in RF propagation), then convergence is guaranteed around 0, since $1 - 2/\alpha$ is never less than -1 .

Next we prove the integration is finite around the singularities of $\log|J_0(y)|$, i. e., the zeroes of $J_0(y)$. It is known that $J_0(y)$ can be expressed in terms of its zeroes, i. e.,

$$J_0(y) = \prod_{i=1}^{\infty} (1 - y^2 / y_i^2) \quad (\text{A3})$$

where y_i is the i th 0 of $J_0(y)$. To verify the integral is finite around y_i , we need only to verify

$\int_{y_i-\delta}^{y_i+\delta} \log|J_0(y)| dy$ is finite when δ is very small, which using the above product expression of the Bessel function, can be written as

$$\int_{y_i-\delta}^{y_i+\delta} \log \left| \prod_{i=1, j \neq i}^{\infty} (1 - y^2 / y_i^2) \right| dy = \int_{y_i-\delta}^{y_i+\delta} \log|1 + y / y_i| dy + \int_{y_i-\delta}^{y_i+\delta} \log|1 - y / y_i| dy \quad (\text{A4})$$

where only the last term may blow up. We then express the last term as

$$\int_{y_i-\delta}^{y_i+\delta} \log|1-y/y_i| dy \sim 2y_i \int_0^{\delta/y_i} \log x dx = (\delta/y_i)(\log(\delta/y_i)-1) \quad (A5)$$

which is finite and thus ends this part of the proof.

Finally we consider the convergence of the integration at infinity. The asymptotic expansion of the Bessel function $J_0(y)$ for large y is

$$J_0(y) \sim \log \sqrt{2/\pi} - \frac{1}{2} \log y + \log \left| \cos(y - \frac{\pi}{4}) \right|. \quad (A6)$$

Consider the integration $\int_Y^\infty y^{-(1+2/\alpha)} \log|J_0(y)| dy$ where Y is a large constant. Using the above asymptotic expansion, we approximate it by

$$\int_Y^\infty y^{-(1+2/\alpha)} \log \sqrt{2/\pi} dy + \frac{1}{2} \int_Y^\infty y^{-(1+2/\alpha)} \log y dy + \int_Y^\infty y^{-(1+2/\alpha)} \log \left| \cos(y - \frac{\pi}{4}) \right| dy$$

(A7)

where obviously the first term converges. We rewrite the second term as

$$\frac{1}{2} \int_Y^\infty y^{-(1+2/\alpha)} \log y dy = -\frac{\alpha}{2} \left[y^{-2/\alpha} \log y \Big|_Y^\infty - \int_Y^\infty y^{-(1+2/\alpha)} dy \right] \quad (A8)$$

which is also bounded. The last term involves the function $\log \left| \cos(y - \frac{\pi}{4}) \right|$ with periodic

singularities. Similarly as before, we can prove the integration $\int_{y_i-\delta}^{y_i+\delta} \log \left| \cos(y - \frac{\pi}{4}) \right| dy$ converges

at any singularity y_i , since the integrand $\log \left| \cos(y - \frac{\pi}{4}) \right|$ at any singularity behaves like

$\log|y - y_i|$ whose integration around y_i is bounded. Now we can set an upper bound for this

integration over any period, i.e., $\left| \int_y^{y+\pi} y^{-(1+2/\alpha)} \log \left| \cos(y - \frac{\pi}{4}) \right| dy \right| < B_0$. We then show that the

last term is bounded by the following inequalities:

$$\left| \int_y^{y+\pi} y^{-(1+2/\alpha)} \log \left| \cos\left(y - \frac{\pi}{4}\right) \right| dy \right| < B_0 \sum_{i=0}^{\infty} (Y + i\pi)^{-(1+2/\alpha)} < B_0 \int_{Y-\pi}^{\infty} y^{-(1+2/\alpha)} dy \quad (\text{A9})$$

which completes the whole proof.

3.7 Section Reference

- [1] William Feller, "An Introduction to Probability Theory and Its Applications," Vol. 2, 1966
- [2] D. Molkdar, "Review on radio propagation into and within buildings," *IEE Proceedings-H*, Vol. 138, No. 1, pp. 61-73, Feb. 1991
- [3] D. C. Cox, R. R. Murray, and A. W. Norris, "800-MHz attenuation measured in and around suburban houses," *Bell Sys. Tech. J.*, 1984, 63, (6), pp. 921-955
- [4] S. E. Alexander, "Characterizing buildings for propagation at 900 MHz," *Electron. Lett.*, 1983, 19, (2), pp. 860

DISTRIBUTION LIST

addresses	number of copies
AIR FORCE RESEARCH LABORATORY/SNDR JAMES HUNTER 25 ELECTRONIC PKY ROME NY 13441-4515	10
UNIVERSITY OF CA BERKELEY ELECTRONIC RESEARCH LABORATORY 253 CORY HALL 1774 BERKELEY CA 94720	5
AFRL/IFOIL TECHNICAL LIBRARY 26 ELECTRONIC PKY ROME NY 13441-4514	1
ATTENTION: DTIC-OCC DEFENSE TECHNICAL INFO CENTER 8725 JOHN J. KINGMAN ROAD, STE 0944 FT. BELVOIR, VA 22060-6218	1
DEFENSE ADVANCED RESEARCH PROJECTS AGENCY 3701 NORTH FAIRFAX DRIVE ARLINGTON VA 22203-1714	1
ATTN: NAN PERIMMER IIT RESEARCH INSTITUTE 201 MILL ST. ROME, NY 13440	1
AFIT ACADEMIC LIBRARY AFIT/LDR, 2950 P. STREET AREA B, BLDG 642 WRIGHT-PATTERSON AFB OH 45433-7765	1
AFRL/MLME 2977 P STREET, STE 6 WRIGHT-PATTERSON AFB OH 45433-7739	1

AFPL/HESC-TDC 1
2698 G STREET, BLDG 190
WRIGHT-PATTERSON AFB OH 45433-7604

ATTN: SMDC IM PL 1
US ARMY SPACE & MISSILE DEF CMD
P.O. BOX 1500
HUNTSVILLE AL 35807-3801

TECHNICAL LIBRARY D0274(PL-TS) 1
SPAWARSSYSCEN
53560 HULL ST.
SAN DIEGO CA 92152-5001

COMMANDER, CODE 4TL0000 1
TECHNICAL LIBRARY, NAWC-WD
1 ADMINISTRATION CIRCLE
CHINA LAKE CA 93555-6100

CDR, US ARMY AVIATION & MISSILE CMD 2
REDSTONE SCIENTIFIC INFORMATION CTR
ATTN: AMSAM-RD-DB-R, (DOCUMENTS)
REDSTONE ARSENAL AL 35898-5000

REPORT LIBRARY 1
MS P364
LOS ALAMOS NATIONAL LABORATORY
LOS ALAMOS NM 87545

ATTN: D'BORAH HART 1
AVIATION BRANCH SVC 122.10
FOB10A, RM 931
800 INDEPENDENCE AVE, SW
WASHINGTON DC 20591

AFIWC/MSY 1
102 HALL BLVD, STE 315
SAN ANTONIO TX 78243-7016

ATTN: KAROLA M. YOURISON 1
SOFTWARE ENGINEERING INSTITUTE
4500 FIFTH AVENUE
PITTSBURGH PA 15213

USAF/AIR FORCE RESEARCH LABORATORY
AFRL/VSOSA(LIBRARY-BLDG 1103)
5 WRIGHT DRIVE
HANSCOM AFB MA 01731-3004

1

ATTN: EILEEN LADUKE/D460
MITRE CORPORATION
202 HURLINGTON RD
BEDFORD MA 01730

1

OUSD(P)/DTSA/DUTD
ATTN: PATRICK G. SULLIVAN, JR.
400 ARMY NAVY DRIVE
SUITE 300
ARLINGTON VA 22202

1

AIR FORCE RESEARCH LAB/SND
25 ELECTRONIC PKY
ROME NY 13441-4515

1

JOANNE L. ROSSI
AIR FORCE RESEARCH LAB/SNW
25 ELECTRONIC PKY
ROME NY 13441-4515

1

ROBERT T. KEMERLEY
AIR FORCE RESEARCH LABORATORY/SND
2241 AVIONICS CIRCLE, RM C2G69
WRIGHT-PATTERSON AFB OH 45433-7322

1